

UW-Madison.

MET Publication No.91.05.W1.

Collected Abstracts and Viewgraphs

9th Meeting of the Midwest Association of Cloud and Aerosol Physics (MACAP)

May 16-17, 1991

at Madison, Wisconsin

Pao K. Wang, Editor

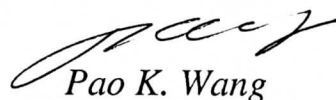
THE SCHWERTFEGER LIBRARY
1225 W. Dayton Street
Madison, WI 53706

Foreword

This is the collected abstracts and viewgraphs presented in the 9th Meeting of the Midwest Association of Cloud and Aerosol Physics (MACAP), May 16-17, 1991, held at Madison, Wisconsin. It was my great pleasure to welcome you all to Madison. I feel better and better about our meeting each time and enjoyed listening to all the papers. I want to thank the session chairmen who were responsible for the orderly progress of the meeting.

As you remember, this meeting was also coincident with the retirement of our friend Roscoe Braham. Roscoe gave the opening talk on the "45 years of cloud physics at Chicago" and I believe everyone would agree with me that it was a fascinating talk. I hope Roscoe can put it in written form someday and have it published in the AMS Bulletin for it is an important piece of history of cloud physics in U.S.

In this volume, I have put the page number right after the title of the paper. Those without a page number indicate that abstracts are not available. In some cases, the title and the order of the authors are not completely consistent with that listed in the program. But I did not alter them in either place. Mr. Dan Johnson has helped in putting this volume together.



Pao K. Wang

December 1991

9th MEETING

MIDWEST ASSOCIATION OF CLOUD AND AEROSOL PHYSICS

MAY 16 - 17, 1991
 Room B1B, Lowell Hall, Univ. of Wisconsin
 MADISON, WISCONSIN

MAY 16 (THURSDAY)

8:20 WELCOME (Pao Wang)

8:30-9:15 45 years of cloud physics at Chicago
Roscoe Braham (U. Chicago) (invited)

SESSION 1	AEROSOL PHYSICS - I (John Carstens)
------------------	--

9:15-9:40 Cloud chamber modeling with fluid dynamic code
 FIDAP
Allen Williams (Ill. Water Survey)

9:40-10:05 Cloud chambers for chemical analysis of condensation
 nuclei....(P.1)
*Alofs, Hagen, White, Hopkins, Trueblood, & Williams (U.
 Missouri-Rolla & Ill. Water Survey)*

10:05-10:30 Achieving subsaturated initial condition in an expansion
 cloud chamber....(P.10)
John Schmitt (U. Missouri-Rolla)

10:30-10:45 Coffee Break

SESSION 2	AEROSOL PHYSICS -II (Ted Green)
------------------	--

10:45-11:10 A laboratory liquid fuel burner and the properties of the
 associated combustion aerosols
*Holland, Jacquin, Trueblood, Hagen, Whitefield (U.
 Missouri-Rolla)*

11:10-11:35 Modelling the filtration of aerosol particles by
 multilayered fibrous media....(P.12)
Zhili Liu & Pao Wang (U. Wisconsin-Madison)

11:35-12:00 Convective particle transport - Double diffusion
 aspects....(P.17)
Ted Green (U. Wisconsin-Madison)

12:00-1:20 Lunch

SESSION 3		CLOUD MICROPHYSICS - I (Ken Beard)	
1:20-1:45	Calculations of the growth rates of hexagonal plate and broad-branch ice crystals <i>Wusheng Ji & Pao Wang (U. Wisconsin-Madison)</i>		
1:45-2:10	The influence of drop supercooling on coalescence.....(P.20) <i>Bob Czys (Ill. Water Survey)</i>		
2:10-2:35	Satellite monitoring of oil-fires in Kuwait expedition (SMOKE). <i>Sanjay Limaye (U. Wisconsin - Madison)</i>		
2:35-3:00	Representation of cloud microphysical processes in warm rain models - A new approach.....(P.25) <i>Phil Brown (Trinity College)</i>		
3:00-3:15	<i>Coffee Break</i>		
SESSION 4		CLOUD MICROPHYSICS - II (Phil Brown)	
3:15-3:40	Field experiments of raindrop oscillations <i>Ali Tokay & Ken Beard (U. Illinois-Urbana Champaign)</i>		
3:40-4:05	On the temperature of rain during the St. Valentine's Day ice storm.....(P.30) <i>Bob Czys (Ill. Water Survey)</i>		
4:05-4:30	Charge and humidity effects on coalescence <i>Donna J. Holdridge (Ill. Water Survey)</i>		
SESSION 5		MESOSCALE CLOUDS (Harry Ochs)	
4:30-4:55	An overview of the Winter Icing & Storms Project (WISP) <i>Roy Rasmusson (NCAR)</i>		
4:55-5:20	Some preliminary analysis of the physics of winter clouds during WISP-1990.....(P.35) <i>Doug Streu and Pao Wang (U. Wisconsin-Madison)</i>		
5:20-5:45	Do we have good roll models ?.....(P.40) <i>Dave Kristovich (U. Chicago)</i>		
7:00	<i>Dinner (Imperial Garden)</i>		

MAY 17 (FRIDAY)

SESSION 6	CLOUD OBSERVATIONS & MODELLING - I (Roy Rasmusson)
------------------	---

- 8:30-8:55 Regarding the behavior of merging radar echo cores.....(P.45)
Nancy Westcott (Ill. Water Survey)
- 8:55-9:20 Heat and water budget for a lake effect snow storm.....(P.50)
Roscoe Braham and S. Zhang (U. Chicago)
- 9:20-9:45 Adsorption of alcohol vapor by NaCl aerosol particles
Hsin-Mu Lin, Pao Wang, & Keng Leong (U. Wisconsin-Madison & Argonne National Lab)

9:45-10:00 *Coffee Break*

SESSION 7	CLOUD OBSERVATIONS & MODELLING (Don Hagen)
------------------	---

- 10:00-10:25 An indirect climatology of Midwest cloudiness.....(P.56)
Mary Peterson (Ill. Water Survey)
- 10:25-10:50 The relative importance of environmental stability, mid-level dry layers, and temperature inversions on radar cloud heights during summer over St. Louis
R. Scott (Ill. Water Survey)
- 10:50-11:15 Cloud dynamical and microphysical processes in simulated CCOPE storm.....(P.61)
Dan Johnson and Pao Wang (U. Wisconsin-Madison)

BUSINESS MEETING (Pao Wang) 11:15-12:00

- (1) Next meeting (2) Abstracts and/or viewgraphs (3) Other business.

Cloud Chambers for Chemical
Analysis of Cloud Condensation Nuclei

By

A. L. Williams
(Illinois State Water Survey)

D. J. Alofs, D. E. Hagen, D. R. White, and A. R. Hopkins
(University of Missouri-Rolla)

The air sample flow rate of 1333 liters per minute is sufficient to collect our CCN sample in 1 to 3 hours. The sample first passes through a stainless steel shell and tube heat exchanger to heat the air such that the wet bulb temperature is about 25°C. The reason for this will be explained later.

Next the air passes through a virtual impactor called impactor #1. Impactor #1 has a 0.5 μm diameter cut point, as do impactors #2 and #3. Virtual impactors are widely used in sampling atmospheric particles for chemical analysis. They are also called dichotomous separators.

The way they work is as follows: This nozzle (point to it) accelerates the inlet air stream to a high velocity (133 meters/second in our case). Ten percent of the air is drawn into the receiver shown here (Point to it). Ninety percent of the air is deflected into this plenum chamber (Point to it). The flow deflection into the plenum chamber causes a sharp bend in 90% of the streamlines. The larger particles cannot make the sharp turn and so their inertia carries them into the receiver. The small particles follow the streamlines so that 90% of the small particles do not go into the receiver and 10% do go in.

The major stream out of the impactor, containing the small particles, goes to a cloud chamber called the "haze chamber." The minor stream, containing the large particles (and 10% of the small particles) goes to filter #1, then through an automatic flow control valve, then to a vacuum blower.

NEXT TRANSPARENCY

The haze chamber consists of 9 vertical aluminum plates 4 feet high by 12 feet long. The plates are spaced 1 cm apart. The sample air flows horizontally in the 1 cm space between the plates. The plates are covered with a cloth wicking material and

are supplied with sufficient water at the top edge to keep their entire surface wet. The temperature of the plates is allowed to float, and a rigorous analysis indicates that the adiabatic plates will be nearly isothermal, at a temperature equal to the wet bulb temperature of the incoming air, i.e., 25°C, because of the preheater.

A brief explanation is that evaporative cooling causes the plates to be colder than the air. Thus heat flows from the air to the plates, such that there is a heat balance at the plates. The result is that the adiabatic plates are nearly isothermal. This provides for simple construction of the haze chamber.

The air reaches 100% relative humidity as it passes through the haze chamber. The CCN grow to become haze droplets. The equilibrium size of a CCN at 100% relative humidity depends only on the critical supersaturation of the CCN. The exact chemical composition does not effect this size.

The haze droplets leaving the haze chamber enter impactor #2. The droplets smaller than 0.5 μm are carried out of the impactor with the major exit stream and pass into a second cloud chamber called the CFD. This stream contains CCN with critical supersaturations larger than 0.16%. Let S_C denote critical supersaturation.

The minor flow exiting impactor #2 passes to filter #2, where the particles are collected for chemical analysis. The particles on this filter we shall name "large CCN." Filter #2 contains particles with $S_C < 0.16\%$ plus 10% by number of the particles with $S_C > 0.16\%$.

Allen Williams is building and experimenting with our impactors, in order to get the minor flow to be less than 10% of the input flow. In one version of an impactor under development, the receiver has a net flow of zero, because clean air is introduced into the receiver to flush the particles out of the receiver and into a small filter. The small size of the filter would make chemical analysis easier. It would also avoid contamination of the course particles by 10% of the fine particles.

NEXT TRANSPARENCY

The continuous flow diffusion chamber, called the CFD, consists of three vertical plates 4 ft high by 12 ft long. The plates are again spaced 1 cm apart, with the air flowing in the 1 cm space between the plates. The plates are covered with cloth wicking material and are wet with water. The inner plate is

heated to 25°C electrically. The outer plates are cooled to 20°C by water jackets.

A 1% supersaturation is produced midway between the plates. Not all the air experiences this maximum supersaturation because the spatial variation of supersaturation between the plates is approximately parabolic, with zero supersaturation at the plates. Fortunately, the velocity profile is also parabolic, so that where the supersaturation is low, the velocity is also low. Thus, about half the volume flow of air experiences nearly the full 1% supersaturation.

Water drops grown on the particles with $S_c < 1\%$ pass into impactor #3 and pass into the minor flow of the impactor. The minor flow is slightly heated, to evaporate the droplets and then passes into filter #3. Filter #3 contains particles in the S_c range 0.1% to 1%. If Allen's improvements on impactor #3 work out, filter #3 will not contain the 10% contamination shown in the transparency.

NEXT TRANSPARENCY

The transparency shows a numerical simulation of the collection system. The individual components are each realistically modeled and then the entire system performance is computed using a Monte Carlo technique. Don Hagen did all the computer programming.

The vertical axis is $dN/d\ln S_c$ where N is particle concentration per cubic cm, and S_c is critical supersaturation. Thus, the figure is a plot of differential particle concentrations as functions of critical supersaturation.

The curve labeled "Total," with diamond symbols, is the assumed distribution of the atmospheric aerosol. This is based on a tri-modal Whitby "grand average continental" size distribution, and an assumption that all the particles contain 50% ammonium sulfate and 50% silica.

Curve #1, with the circles, shows the particles that deposit on filter #1. Curve #1 approaches the "Total" curve for $S_c < 0.02\%$ because this S_c corresponds to 0.5 μm diameter for the chemical composition of the simulation. Impactor #1 delivers all particles larger than 0.5 μm to filter #1. The right side of curve #1 is one decade below the "Total" curve, due to contamination of the minor flow of impactor #1 by 10% of the fine particles.

Curve #2 shows particles on filter #2, which should contain particles with S_c in the range .02% to 0.16%, plus 10% of the

particles with S_c above 0.16%. Curve #2 looks reasonable, bearing in mind that a realistic, finite, resolution of impactors #1 and #2 is used in the model. Note that filter #2 contains some contamination outside the S_c range 0.02% to 0.16%. Thus this filter, which collects the "large CCN," has some contamination, but fortunately, we are most interested in filter #3, which captures the "small CCN."

The curve marked CFD, with the square symbols, is the particle flow going into the CFD cloud chamber, i.e. the major flow out of impactor #2. This curve drops-off very sharply to the left, which is extremely encouraging. This means that filter #3 will contain practically no contamination by particles to the left, (particles of smaller S_c , and larger size). The right hand cut-off for filter #3 will be provided after the particles pass through the CFD and impactor #3. We haven't got that set of processes into our simulation yet.

NEXT TRANSPARENCY

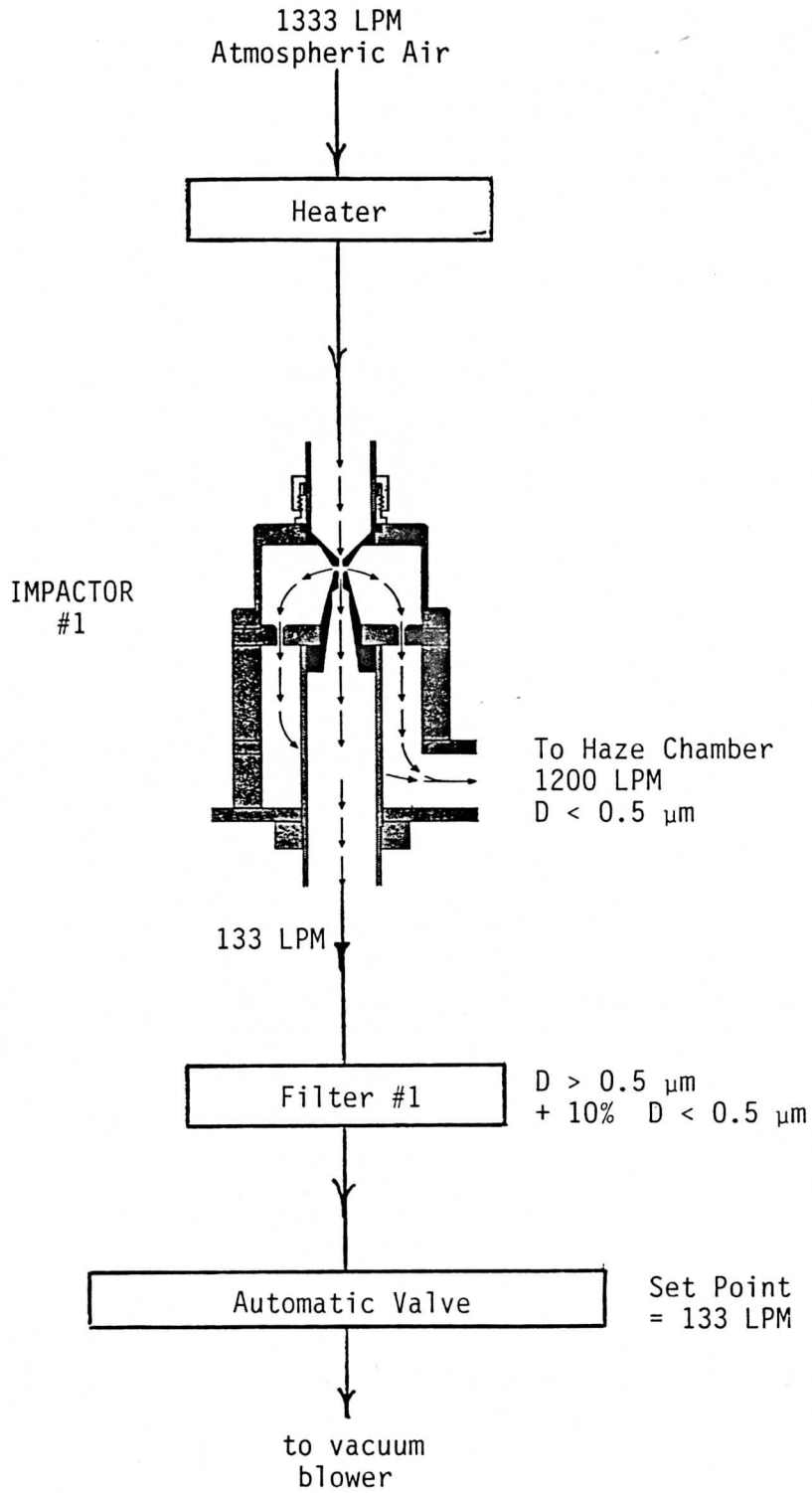
This transparency shows the mass distributions. The distinctions between the four curves is the same as in the previous transparency. Note that the Total curve drops to the right, so that the small CCN are a small part (less than 1%) of the total mass of atmospheric aerosol. Recall from the previous transparency (flip back to it for a moment) that the Total curve rises to the right, which means that the "small CCN" account for most of the CCN by number.

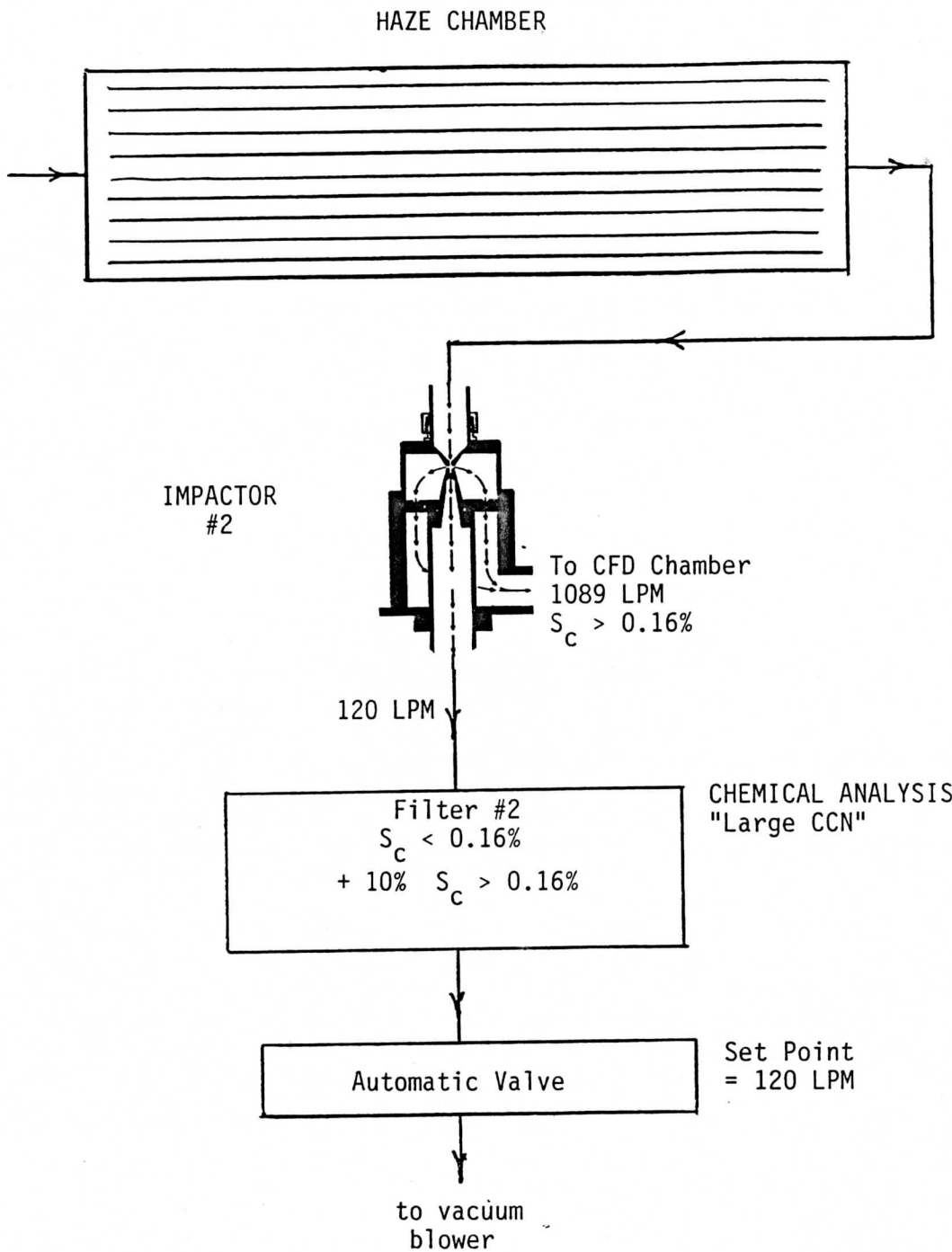
Thus, for applications where the number of CCN is important, as in the case of the radiation effects of clouds, one should focus on the small CCN. However, one must beware because their mass is so small that there is a large risk of contamination (by other particles). To avoid contamination requires very high separation efficiency of the collection system.

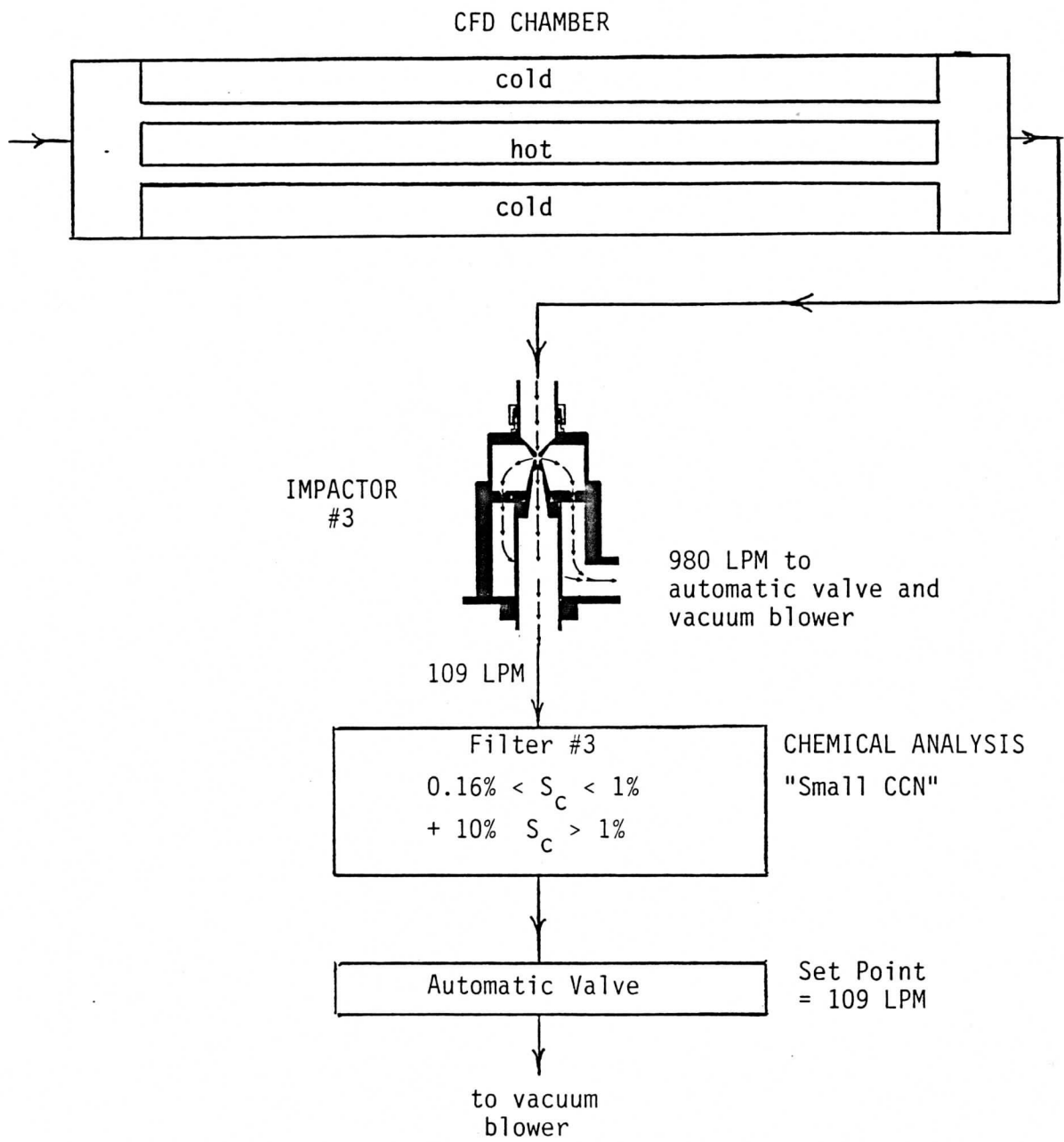
FLIP TO $dm/d\ln S_c$
TRANSPARENCY
again

Note how sharply the left side of the CFD curve drops. We think we are going to avoid contamination of the small CCN by the other particles

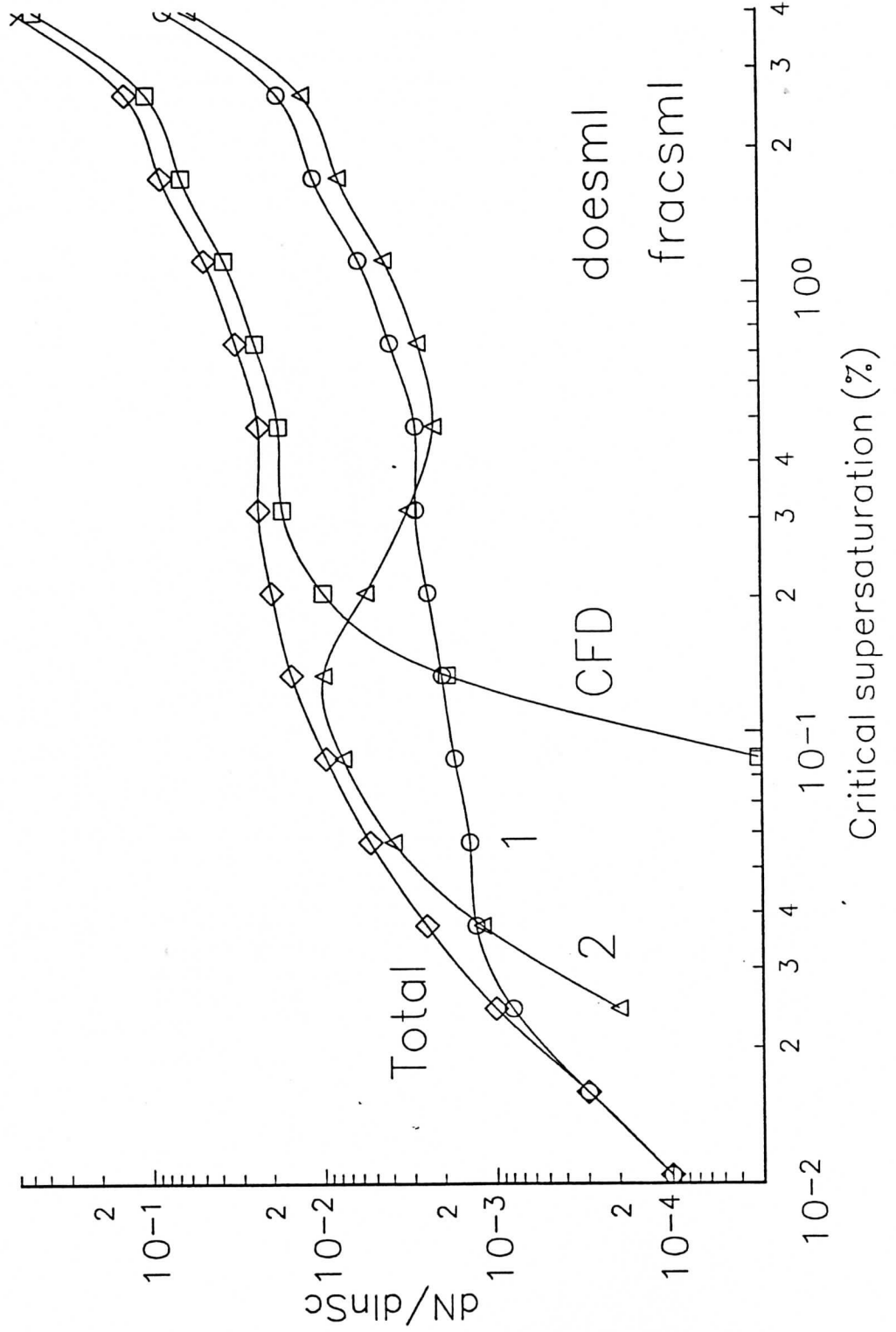
NOTE: The rest of the talk concerns photographs of the cloud chambers as they are being assembled.







DOE CCN model, 4/26/91
 Small slit, impactor 2



ACHIEVING SUBSATURATED INITIAL CONDITIONS IN AN EXPANSION CLOUD CHAMBER

John L. Schmitt
Cloud and Aerosol Sciences Laboratory
G7 Norwood Hall
University of Missouri
Rolla, Missouri 65401

ABSTRACT: The expansion chamber can be started with subsaturated initial conditions and expanded to relatively low supersaturations accompanied by a large change in temperature. To do this one needs a binary mixture in the chamber of water and a material that completely mixes with water and has a very low vapor pressure. One possible group of materials is the glycols. We are measuring the vapor pressures of mixtures of glycols and water to determine their suitability for this application.

Expansion Chamber! 298°K

R. H.	-25°C	-40°C
100%	23	83
80%	19	67
60%	14	51
40%	9.6	35
20%	4.9	18
10%	2.4	<u>8.8</u>
5%	1.2	4.4
2.5%	0.6	2.2
1%	0.3	0.9

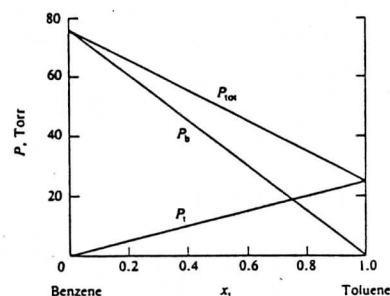
Raoult's Law: Ideal

$$P_i = P_i^{\circ} x_i$$

P_i = pressure over liquid

P_i° = pure liquid

x_i = mole fraction



Glycol	Vapor Pressure
Ethylene Glycol	44.8 KPA 446°K
Diethylene	10.1
Triethylene	2.5
Tetraethylene	0.4

Activity Coefficients:

$$\gamma_i = \frac{P_i}{P_i^0 X_i}$$

γ_i = Act. coeff.

P_i = pressure

P_i^0 = press. pure

X_i = mole fract.

Calculation:

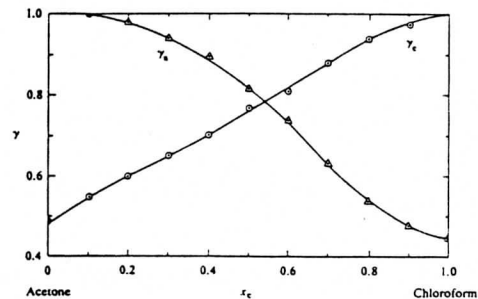
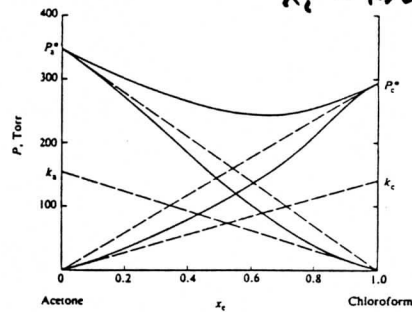
{ 15°C, mole fract. H₂O = 0.025 }
 { extrapolate v.p. Tetra. }

Result: (in vapor)

1 molecule of Tetra.

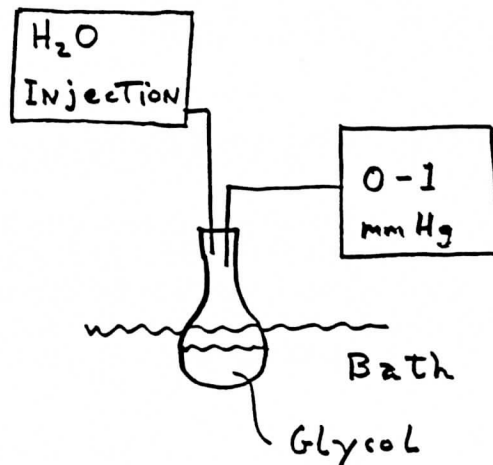
400 molecules of H₂O

Assumption: $\gamma_{gly.} = 1$



Vapor Pressure

Measurements:



MODELLING THE FILTRATION OF AEROSOL PARTICLES BY MULTILAYERED FIBROUS MEDIA

Zhili Liu

Pao K. Wang

Environmental Air Quality Engineering

University of Wisconsin-Madison

1. INTRODUCTION

- As air pollutants, aerosol particles comprise by number the greatest amount of emissions.
- Many air cleaners are large and are ineffective against aerosol particles smaller than some $10\ \mu\text{m}$ diameter. When there is need for efficient, say better than 95%, removal of aerosol particles in the 0.1 to $1.0\ \mu\text{m}$ range of diameter from any substantial flow of air, there is no alternative to the employment of fibrous filters.
- Problems of particle deposition on clean, dustfree fiber constitute the main content of the classical theory of air filtration.
- It can be said that the development of the theory of air filtration on fibrous filters is determined by the achievements of the theory of viscous flow past a system of cylinders.
- The Navier-Stokes equation is the basic dynamical equation expressing Newton's second law of motion for a fluid.

2. DOMAIN DECOMPOSITION METHOD

In applying finite difference methods to a specific problem one of the most important considerations is the design of the finite difference grid. The choice of grid affects many aspects of the finite difference method. The efficiency of the numerical solution algorithm and accuracy of the computed solution are strongly dependent of the finite difference grid. The type of grid can also restrict the choice of the numerical algorithm.

In this research we use the domain decomposition method to solve the filtration problems. To solve the filtration problem we impose several polar finite difference grids near the fibers and superimpose on these grids some Cartesian difference grids. The inner boundary of the Cartesian grids are inside the polar grids. The outer boundaries of the Cartesian grids lay outside the polar grids.

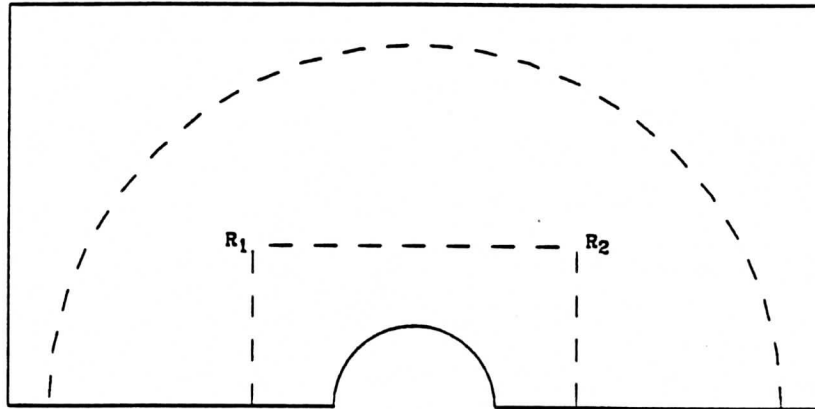


Fig. 1. Domain Decomposition Method.

3. NUMERICAL RESULTS

We investigate the viscous flow past an infinite circular cylinder first. We then study single array model of fibrous filters.

1. The model of viscous flow past an infinite circular cylinder.

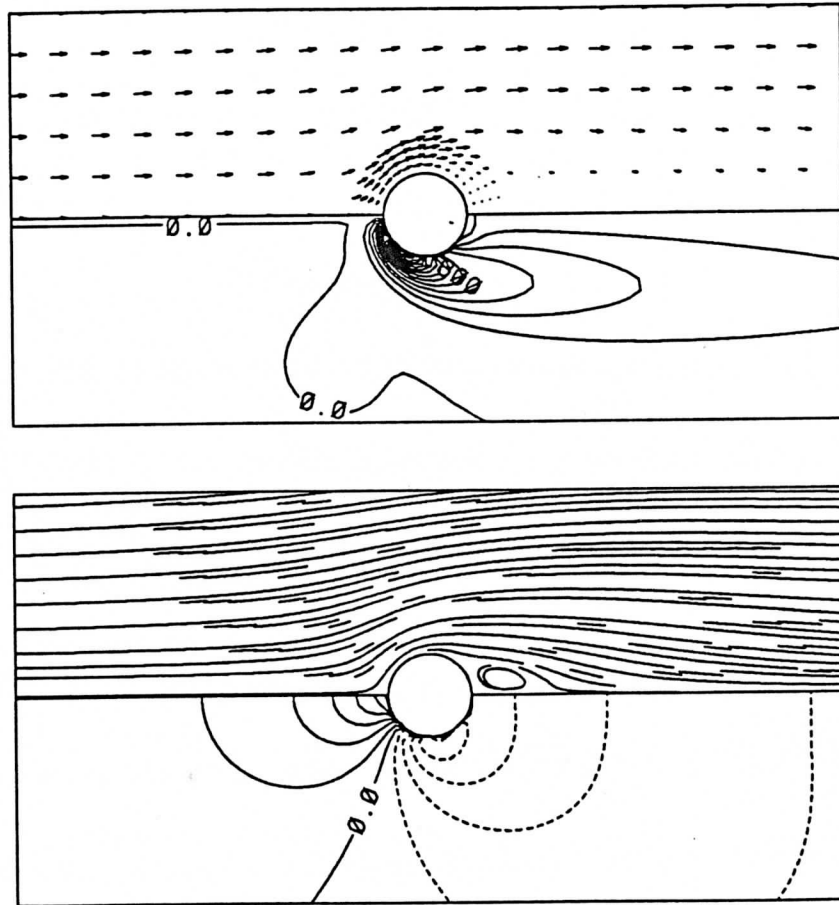
The viscous flow field, which includes velocity vector, streamline, vorticity and pressure distribution, is shown in Fig. 2. Fig. 3 and Fig. 4 show the vorticity and pressure coefficient distribution on the surface of the cylinder, respectively.

2. The model of viscous flow past a single array of circular cylinders.

The vorticity and pressure coefficient distribution on the surface of the cylinder are shown in Fig. 5 and Fig. 6, respectively. The results show that increasing the Reynolds number has the similar effect of decreasing the distance between the cylinders.

4. CONCLUSIONS

1. The domain decomposition method is very accurate for this research.
2. The L.S.O.R. method is very accurate and efficient for the polar grids.
3. The minus vorticity on the surface of the cylinders increases as the Reynolds number increases or the distance between the cylinders decreases.
4. The pressure coefficient on the surface of the cylinder increases as the Reynolds number decreases or the distance between the cylinders increases.



Re=20.0.

Fig. 2. The viscous flow field including velocity vector and negative vorticity distribution (upper), and streamline and pressure coefficient distribution (lower) at the different Reynolds numbers.

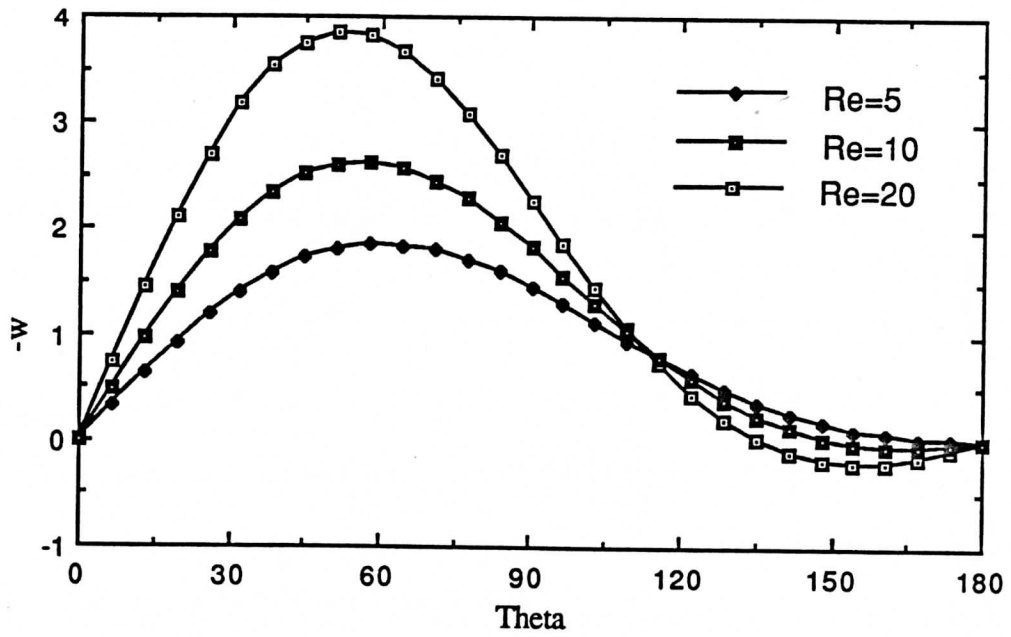


Fig. 3. Vorticity distribution over the surface.

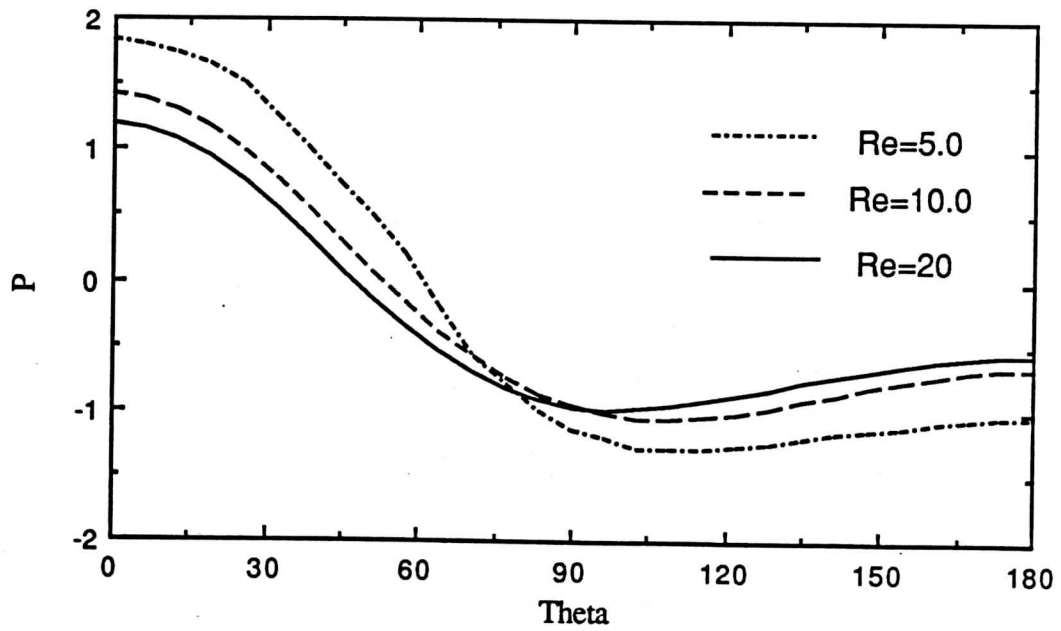


Fig. 4. Pressure coefficient on the surface.

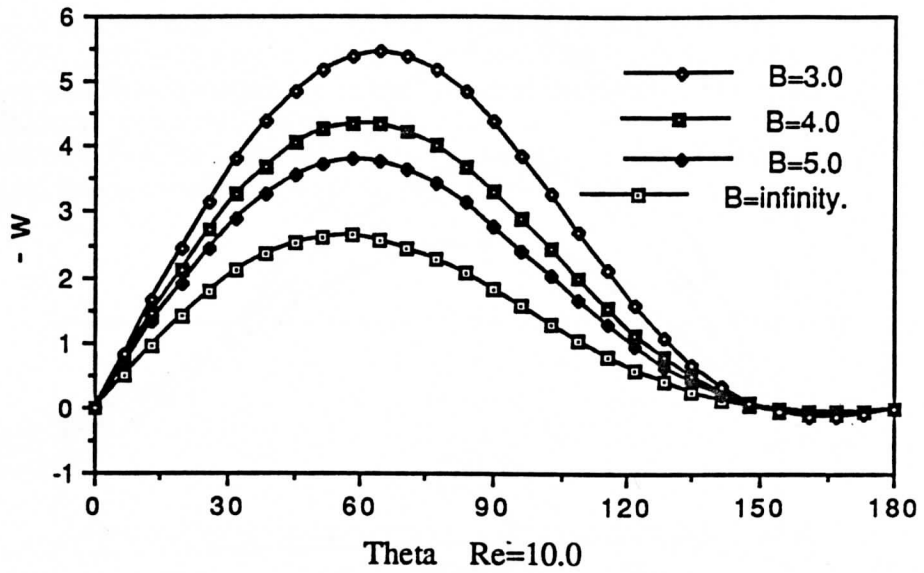


Fig. 5. Vorticity distribution over the surface.

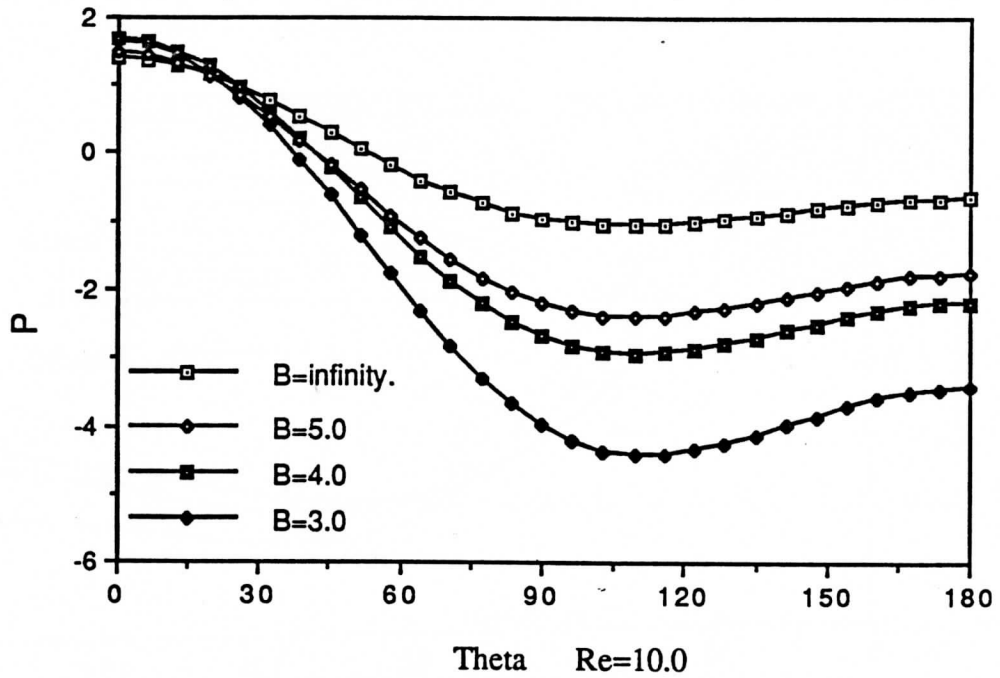


Fig. 6. Pressure coefficient on the surface.

CONVECTIVE PARTICLE TRANSPORT:

Some Double Diffusive Aspects

**Theodore Green III
Departments of Civil and
Environmental Engineering, and Meteorology
University of Wisconsin-Madison**

The vertical transport of small particles is of obvious importance in many cases of atmospheric pollution. While this often occurs by turbulent diffusion or washout during rain events, there are times when air layers containing particles are quiescent, and in a gravitationally stable state. Stokes transport can then dominate, and the vertical transport of very small particles can be quite small. However, even a gravitationally stable suspension can be quite rapidly dispersed, by convective processes. One such process is analogous to that known to oceanographers as "salt fingering", which has been shown to be capable of accounting for much of the vertical salt transport in the world ocean. In this brief paper, I suggest that a similar process in which suspended particles (in air) behave similarly to dissolved salt (in water) may be sometimes important in the atmosphere.

The principle behind the mechanism was apparently first noted by Arons in the mid 1950's (Arons, 1981). Since that time, the effects have been well studied, most notably by Turner (1985), Stern, Huppert, and their associates. A straightforward adaptation to suspensions in air (rather than solutions in water) is as follows. Consider as a very simple model a sharp horizontal interface with warm, particle-containing air above, and clear, cooler air below. The upper suspension is less dense than the lower, clear air, so that the situation is gravitationally stable.

However, the situation is dynamically unstable. To see this, consider a wavy

perturbation of the interface. The downward-moving portions of the upper suspension will lose their heat to the surrounding clear air much more quickly than they lose their particles (which diffuse by Brownian motion). These downward-moving portions then become heavier than the surrounding clear air, and continue to fall. At least in water, long, thin fingers form, and result in a substantial vertical particle flux. Such "sediment fingers" in water have been clearly demonstrated by the experiments reported by Houk and Green (1973), Green and Schettle (1986) and Mogahed (1991).

Order-of-magnitude criteria for the importance of such an atmospheric fingering process can be found by neglecting the interaction between convective motions and Stokes settling, assuming that the experimental flux results found in water also apply in air (with the obvious changes in density, viscosity and molecular diffusion), and following the arguments of Green (1987). In short, one asks if convective instability will even occur at the sharp interface described above, if the resulting fluxes will be much larger than those due to Stokes settling, and if the continuum assumption will apply to the sediment fingers. One finds that the first and third of these criteria are almost certainly satisfied save for extremely dilute suspensions (which, of course, are also of great interest). The second criterion is usually most restrictive, and in air leads to the requirement that

$$N^{1/3} \gg 10^5 d \quad (\text{cgs units})$$

where d is the particle diameter (assumed uniform), and N is the number density. Here, the density of the material making up the particles is taken to be about 1 g/cm^3 .

For example, for $d = 0.1 \mu (10^{-5} \text{ cm})$, N must be about 10^3 cm^{-3} . This is not extremely large, and could well occur at an inversion where airborne particles are trapped. Thus, the fingering phenomenon may indeed be important to atmospheric pollution.

It should be noted that oceanic salt fingering was once regarded as a curiosity, and the fingers far too fragile to withstand even sporadic turbulence. This view has been shown to be incorrect, in a rather dramatic fashion. Could this chronology of perception also occur in meteorology? Perhaps not, but the idea seems to at least deserve consideration.

References

- (1) Arons, A.B., 1981. "The Scientific World of Henry Stommel," in Evolution of Physical Oceanography (Warren and Wunsch, editors).
- (2) Hook and Green, 1973. Suspension Fingers, Deep Sea Research, 20, pp. 757-761.
- (3) Green and Schettle, 1986. Vortex Ringers Associates with Strong Double-Diffusive Fingers, Physics of Fluids, 29, 2109-2112.
- (4) Green, 1987. The Importance of Double Diffusion to the Settling of Suspended Material, Sedimentology, 34, 319-331.
- (5) Mogahed, E.S., 1989. Theoretical and Experimental Investigation of Double-Diffusive Instability at a Sharp Interface. University of Wisconsin-Madison Ph.D. Dissertation, 141 pp.
- (6) Turner, J.S., 1985. Multicomponent Convection, in Annual Review of Fluid Mechanics, Volume 17.

**Laboratory And Field Data
Related To
Supercooled Drizzle And Raindrops
In
Precipitation Processes**

Robert R. Czys
and
Mary Schoen Petersen

Illinois State Water Survey
Atmospheric Sciences Division
Champaign, Illinois

OVERVIEW

1. Drop Supercooling and Coal. Eff.
2. Observational Evidence for CF
3. First Ice and Supercooled Rain Drops

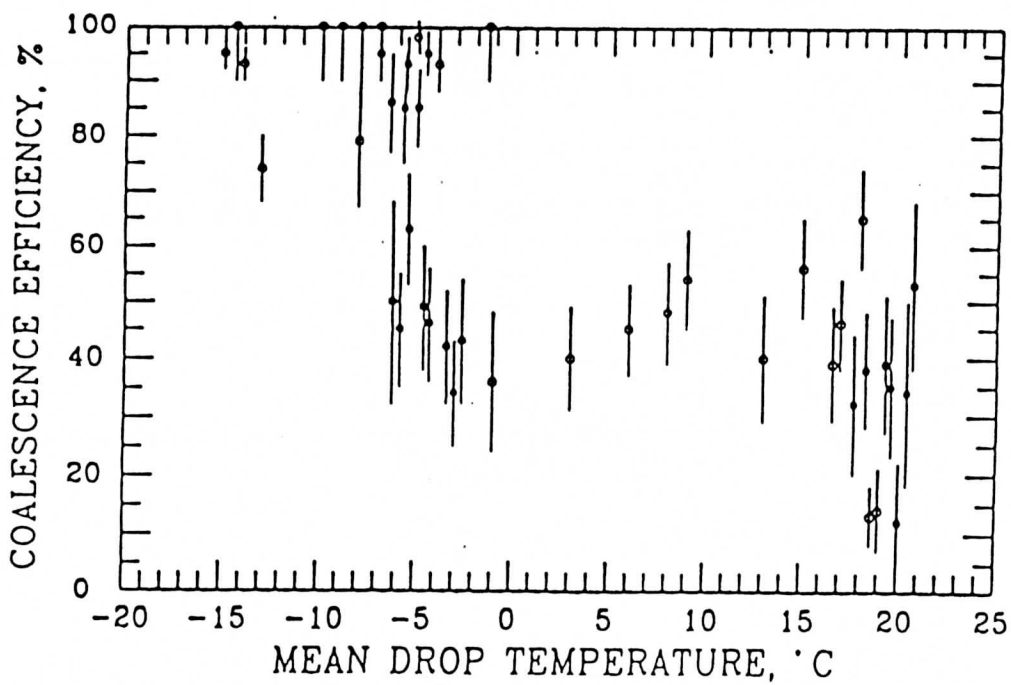
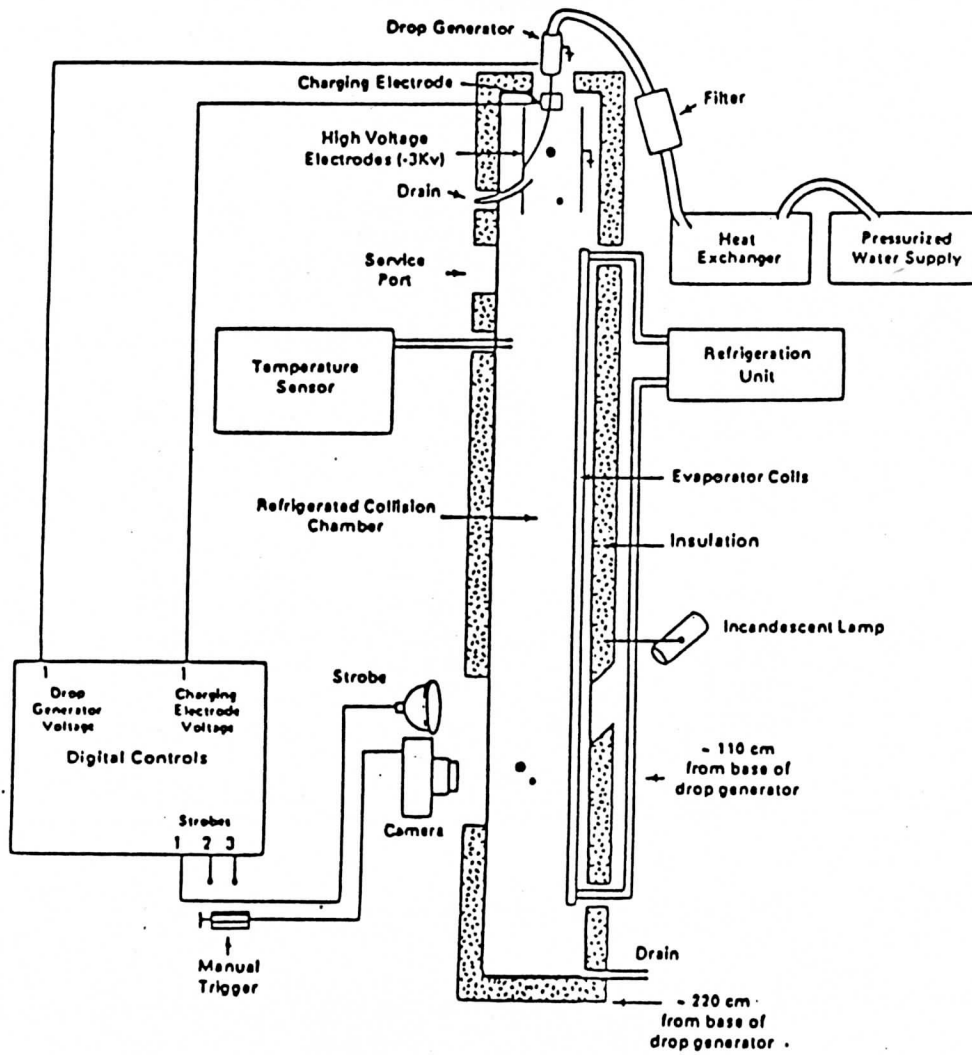


Table 3. Temperature Dependence of Collision Parameters for drops 350 μm and 300 μm radius.

Temp. °C	σ	V_L m s^{-1}	V_S m s^{-1}	ΔV m s^{-1}	WE	P mb
20	73.0	291.7	249.2	42.5	0.74	950
15	73.8	291.4	249.0	42.4	0.73	950
10	74.6	291.0	248.8	42.2	0.72	950
5	75.3	290.6	248.6	42.0	0.70	950
0	76.1	290.2	248.4	41.8	0.69	950
-5	76.9	289.8	248.1	41.7	0.68	950
-10	77.7	289.3	247.8	41.5	0.66	950
-15	78.4	288.8	247.6	41.2	0.65	950
-20	79.2	288.2	247.2	41.0	0.64	950
Δ	8.5	-1.2	-0.8	-3.4	-13.5	

Table 4. Temperature and Pressure Dependence of Collision Parameters for drops 350 μm and 300 μm radius.

Temp. °C	σ	V_L m s^{-1}	V_S m s^{-1}	ΔV m s^{-1}	WE	P mb
20	73.0	291.7	249.2	42.5	0.74	950
15	73.7	302.3	258.1	44.2	0.79	850
10	74.6	314.7	268.5	46.2	0.86	750
5	75.3	329.5	280.9	48.6	0.94	650
0	76.1	337.9	288.0	49.9	0.98	600
-5	76.9	347.2	295.8	51.4	1.03	550
-10	77.7	357.8	304.7	53.1	1.09	500
-15	78.4	369.8	314.8	55.0	1.16	450
-20	79.2	383.8	326.5	57.3	1.24	400
Δ	8.5	32	31	35	68	

Freezing of Supercooled Water Droplets due to Collision

A. J. ALKEZWEENY

Meteorology Research, Inc., Alhambra, Calif.
14 July 1969 and 3 September 1969

JAM, 1969: 8, 194

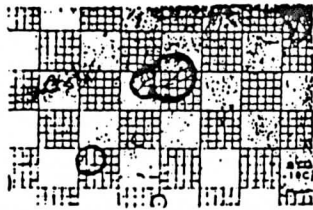


FIG. 1. Droplets of 200 and 140 μm frozen on contact.

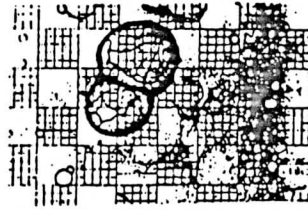
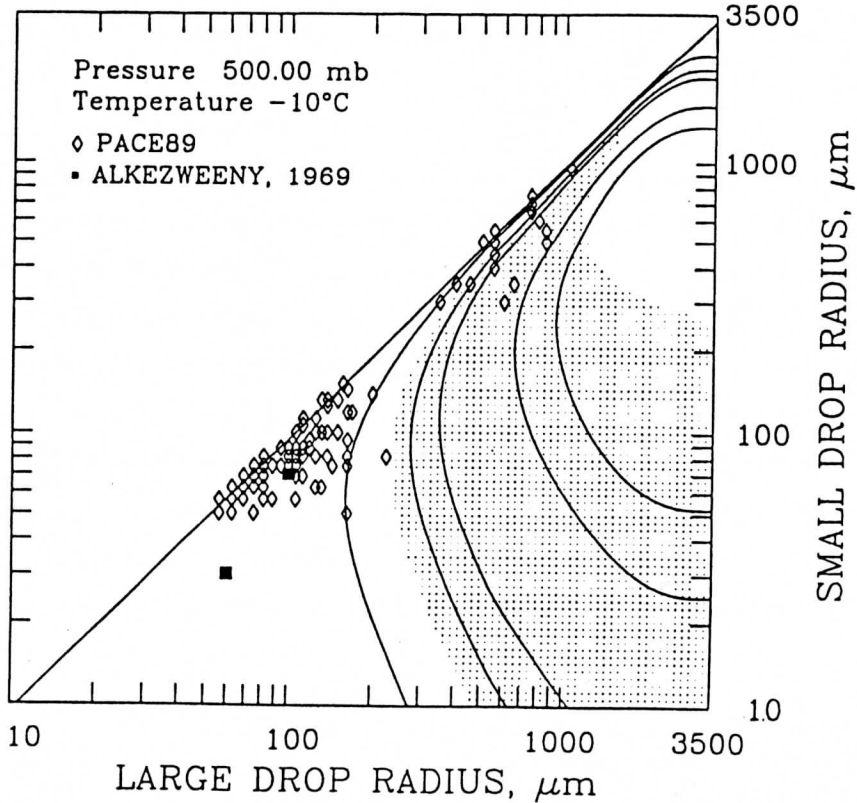


FIG. 2. Droplets of 120 and 60 μm frozen on contact.

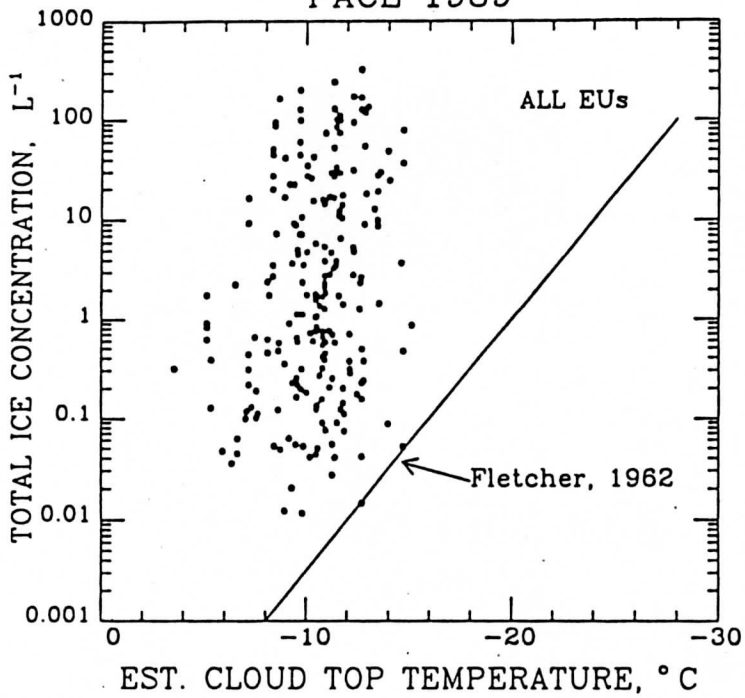
TIME	PRES	ALT	VOR/DME	LATA	LONG	HDG	IAS	TAS	RSHT	RFT	DEW	Q	THETA	TH-E	LWC	FMC	VW	CONC	DBAR	ZDC	ZDP	FL
172414	487	5760	208/39	33.497	88.670	323	126	89.6	-9.4	-0.2	-24.2	1.1	323.9	327.4	0.45	0.71	2.4	198.5	14	6.5	8.1	0



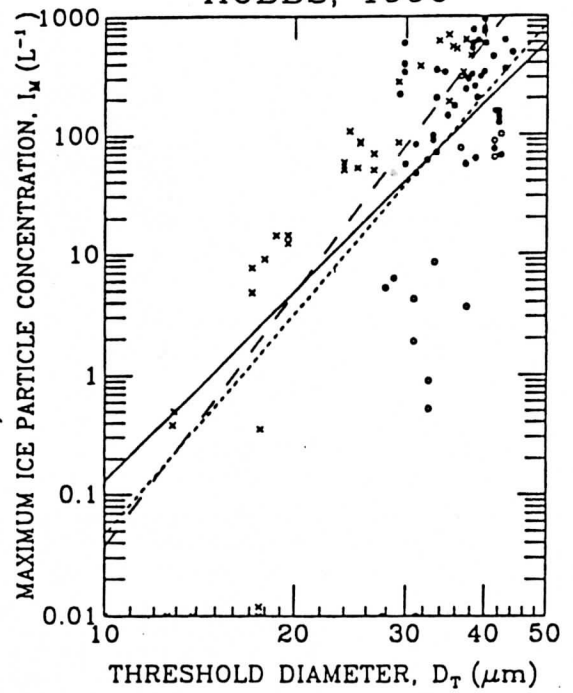
TIME	PRES	ALT	VOR/DME	LATA	LONG	HDG	IAS	TAS	RSHT	RFT	DEW	Q	THETA	TH-E	LWC	FMC	VW	CONC	DBAR	ZDC	ZDP	FL
152705	498	5600	278/62	40.172	89.554	284	126	88.5	-8.7	-7.1	-7.7	4.3	322.8	336.2	0.07	0.37	0.9	128.5	13	0.3	21.8	0



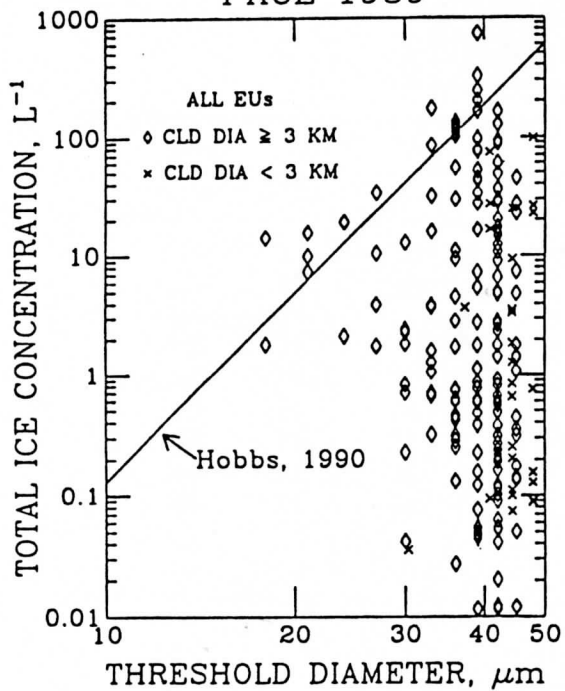
PACE 1989



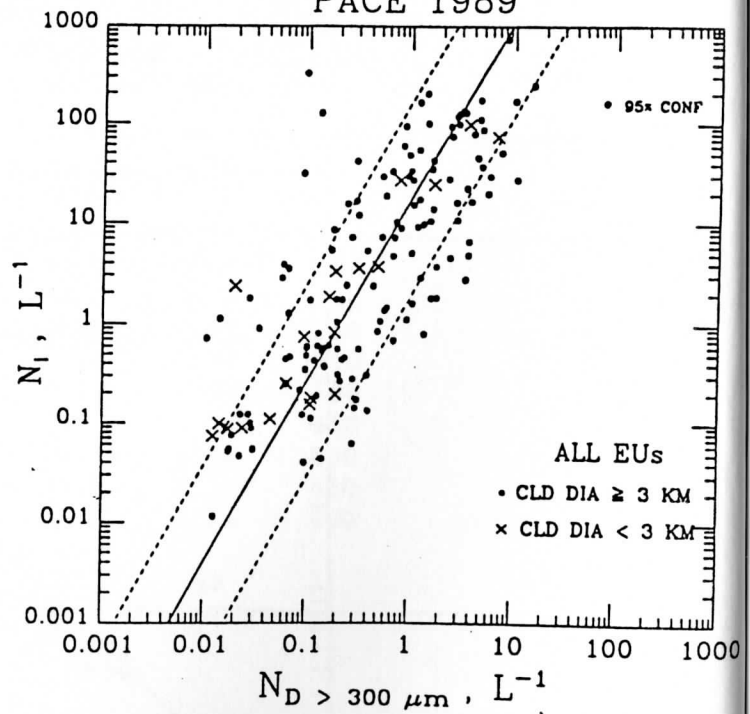
HOBBS, 1990



PACE 1989



PACE 1989



"Representation of Cloud Microphysical Processes
in Warm-Rain Models: A New Approach"

by

Philip S. Brown, Jr.
Trinity College, Hartford, CT

Over the years, cloud modelers often have raised the question, "How can we incorporate cloud microphysics in warm-rain models without actually solving the cloud microphysics equations?" When drop coalescence and breakup are taken into account, detailed calculation of the drop spectrum at every grid point in the cloud or rain shaft remains a formidable computational task. Some modelers (e.g., Clark, 1973 [Viewgr.1]) have carried out such calculations in accounting for condensation and coalescence, but few, if any, have incorporated collision-breakup with the same degree of detail. The root of the problem is that breakup introduces an extra dimension to the calculation of the drop spectrum: if two drops collide and coalesce the result is a single drop; if two drops collide and break apart, the result is a collection (spectrum) of many different-sized fragments (Low and List, 1982 [Viewgr.2]).

We can see how the problem is reflected in the mathematics by looking at the combined coalescence-breakup equation [Viewgr.3]. Here, n is the number density of drops of mass m , while B and C represent the breakup and coalescence terms, respectively. It is seen that the production of drops of mass m by coalescence is represented by a single integral that accounts for all drop pairs whose masses sum to m . The production of drops of mass m by breakup is represented by a double integral that accounts for all drop pairs whose masses sum to a value greater than m .

Numerical solution of the coalescence-breakup equation is carried out by partitioning the drop-size range into categories or "bins" in order to replace the integrals with sums [Viewgr.4]. Here n_i is the number density in bin i , and I is the total number of categories, say, 30-40. A major problem in dealing with this system lies in calculating the coefficients α and β . Their accurate calculation requires evaluation of hundreds of multiple integrals using very high resolution.

To avoid the difficulties of solving just the coalescence part of the equation, many cloud modelers have turned to the convenient bulk parameterization of Kessler (1969). In Kessler's approach, the raindrop size

distribution is assumed to maintain Marshall-Palmer form throughout the process [Viewgr.5]. Cloud water is transferred to rainwater through some rough but easy-to-solve differential equations for autoconversion and accretion. N_0 remains fixed while Λ varies in accordance with the rainwater content.

Berry and Reinhardt (1974) tried to improve upon the Kessler method by developing a parameterization based on accurate numerical solution of the coalescence equation. They also assumed a special form for the drop-size distribution, viz., a pair of gamma distributions each of which is characterized by a single peak [Viewgr.6]. The raindrop peak develops in location, size and breadth according to a Kessler-like formula for autoconversion and other formulas for accretion and hydro-meteor self-collection. Lee and Hong (1987) proposed a parameterization that removes any restrictive assumptions about the particular shape of the drop spectrum. In their approach multiple regression formulas were developed for autoconversion and accretion using cloud-model output to determine the regression coefficients.

Ideally, we would like to have an analytic solution to the coalescence/breakup equation, so that for any initial drop distribution we could simply apply a formula to calculate the drop spectrum at any later time. Analytic solutions have been found to the coalescence equation (Scott, 1960) and to the breakup equation (Feingold, et al., 1988), but only for special cases that are not necessarily realistic. Srivastava (1978) used an analytic approach to obtain an exponential solution to the coalescence/breakup equation under the assumption that each breakup results in a fixed number of fragments. The Marshall-Palmer-type spectrum evolves in accordance with prediction formulas for both Λ and N_0 .

All of the above techniques provide some convenient description of the rain process at the expense of some accuracy. The technique that I would like to propose is no exception. The difference between this technique and the others is that it is designed to reproduce much of the detail found in high-resolution numerical solutions of the coalescence/breakup equation. The advantages of the technique can be summarized as follows [Viewgr.7].

- i) coalescence and breakup are included
- ii) the exact kernel and fragmentation distributions are used
- iii) arbitrary initial drop spectra can be used

and

- iv) the parameterized drop spectrum approaches the "exact" equilibrium.

The disadvantages lie in the two simplifications used to obtain the analytic solutions: the equations are linearized, and only a few categories are used to resolve the drop spectrum.

To show how the solution is obtained, we return to the original differential equations [Viewgr.4] that govern the drop spectrum, but now take the number of bins to be small, say, $I = 2, 3$ or 4 . If we integrate these equations in time for a sufficiently long period, the solution will approach equilibrium. Viewgr.8 shows the high-resolution multi-peaked equilibrium along with its three-bin counterpart. Once the three-bin equilibrium has been determined, the right-hand side of the coalescence-breakup equations (4) can be expanded in a Taylor series about the equilibrium position. For the three-bin case we obtain the equations shown in Viewgr.9. Also shown in the View Graph is the simple analytic solution to these equations -- two damped exponential components superimposed on the equilibrium value. The coefficients c_1 and c_2 are determined by the initial spectrum, which is arbitrary. The v_{ij} 's and the decay rates μ_j can be calculated once and for all for a drop spectrum with prescribed mass. By scaling the n_{eq} 's and the μ 's in proportion to the water mass, the solution can be adjusted to allow arbitrary liquid water content. (Tabular values of two sets of the parameters are given by Brown, 1991.)

The exponential solution tells us how the spectrum will evolve toward equilibrium in each of the three drop-size bins. We'd like to enhance this coarse-resolution result to obtain a more accurate representation of the evolving drop spectrum. Let's assume the approximation in Viewgr.10 holds. The idea is to impart the coarse-grid behavior to the fine-grid spectrum by letting the departure from equilibrium go to zero in the same fashion. Viewgr.11 shows the evolution of the drop spectrum computed by high-resolution numerical solution of the coalescence-breakup equation (upper curves) and by application of the approximation technique using a four-bin model with an enhancement assumption slightly different than the one just shown. The parameterization technique is seen to be quite accurate. Ongoing work is aimed at modifying the procedure to take evaporation into account.

Berry, E.X. and R.L. Reinhardt, 1973: Modeling of Condensation and Collection within Clouds. Tech. Rpt. Series P, No. 16, Desert Research Institute, Reno, NV, 96 pp.

Brown, P.S., Jr., 1991: Parameterization of the evolving drop size distribution based on analytic solution of the linearized coalescence-breakup equation. *J. Atmos. Sci.*, 48, 200-210.

Clark, T.L., 1973: Numerical modeling of the dynamics and microphysics of warm cumulus convection. *J. Atmos. Sci.*, 30, 857-878.

Feingold, G., Tzivion, S., and Z. Levin, 1988: Evolution of raindrop spectra. Part 1: Solution to the stochastic collection/breakup equation using the method of moments. *J. Atmos. Sci.*, 45, 3387-3399.

Kessler, E., 1969: On the distribution and continuity of water substance in atmospheric circulations. *Meteor. Monogr.*, No. 32, Amer. Meteor. Soc., 84 pp.

Lee, I.Y. and M.S. Hong, 1987: A Review of Parameterizations of Microphysical Processes in Clouds for Application in Models of Regional Atmospheric Deposition. Rpt. ANL-87-32, Argonne National Laboratory, Argonne, IL, 46 pp.

Low, T.B., and R. List, 1982: Collision, coalescence and breakup of raindrops. Part II: Parameterization of fragment size distributions. *J. Atmos. Sci.*, 39, 1607-1618.

Scott, W.T., 1968: Analytic studies of cloud droplet coalescence. *J. Atmos. Sci.*, 25, 54-65.

Srivastava, R.C., 1978: Parameterization of raindrop size distributions. *J. Atmos. Sci.*, 35, 108-117.

$$\frac{\partial n(m)}{\partial t} = B + C \tag{1}$$

where the breakup term B has the form

$$B = \int_{m/2}^m \int_0^u n(u) n(u_1) f(u, u_1) \{1 - E(u, u_1)\} Q(m; u, u_1) du_1 du - \int_0^m n(m) n(u_1) f(m, u_1) \{1 - E(m, u_1)\} du_1 \tag{2}$$

and the coalescence term C is

$$C = \int_0^{m/2} n(u) n(m-u) E(u, m-u) du - \int_0^m n(m) n(u) E(u, m) du \tag{3}$$

where

- $n(m)$ = number density for drops of mass m ($n(m)$ is time dependent)
- t = time
- $E(u, u_1)$ = coalescence efficiency for drops of masses u, u_1
- $Q(m; u, u_1) \Delta m$ = average number of fragments of mass m to $m + \Delta m$ produced by collision and subsequent breakup of drops of masses u, u_1
- $f(u, u_1) = \pi(r_u + r_{u_1})^2 E_1(u, u_1) |\Delta V(u, u_1)|$
- r_u = radius of a drop of mass u
- E_1 = collision efficiency
- $\Delta V(u, u_1)$ = difference in terminal velocities of u - and u_1 -drops

In the calculations performed for this study, we have used the formulas of Low and List (1982 a,b) to calculate the coalescence efficiency E and the fragment distribution function Q .

Viewgraph 3.

$$\frac{dn_i}{dt} = \sum_{j,k} \alpha_{ijk} n_j n_k - n_i \sum_k \beta_{ik} n_k \tag{4}$$

$i = 1, \dots, I$

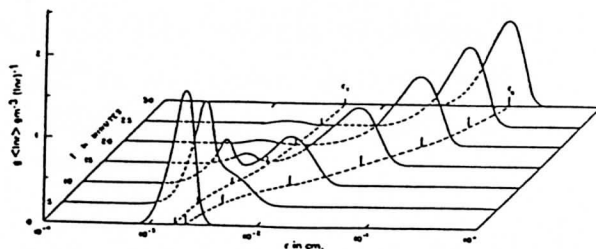
where n_i represents the mass-weighted average of $n(m)$ over the interval (m_i, m_{i+1}) and where the coefficients α_{ijk}, β_{ik} account for the gain and loss, respectively, of drop concentration due to the combined effects of coalescence and breakup.

Viewgraph 4.

$$n(D) = N_0 e^{-\lambda D} \tag{5}$$

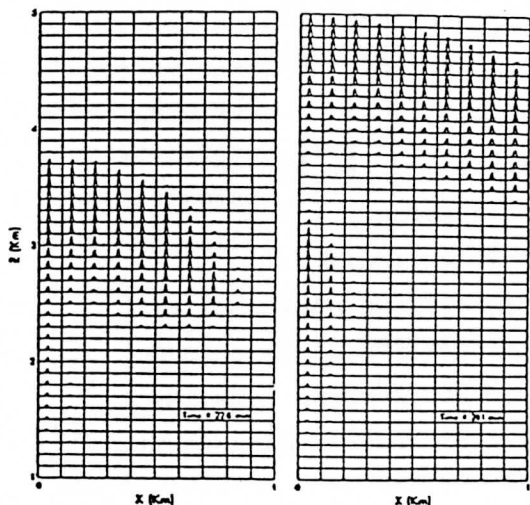
where D denotes drop diameter, N_0 has the constant value of $8 \times 10^{-4} \text{ mm}^{-3}$ and varies with rainwater content

Viewgraph 5.



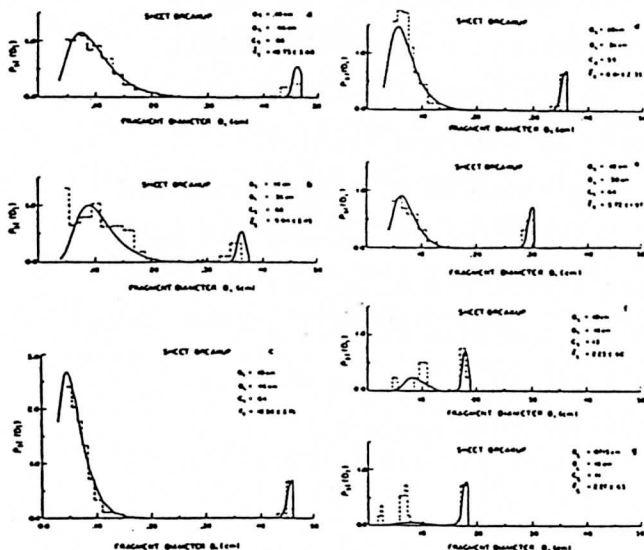
Viewgraph 6.

(From Berry and Reinhardt, 1973)



Viewgraph 1.

(From Clark, 1973)



Viewgraph 2.

(From Low and List, 1982)

I. Representation of Coalescence

A. Parameterization Based on:

1. Kessler's formulas (Marshall-Palmer spectrum)
2. Numerical solutions
 - a. Berry (gamma distributions)
 - b. Lee (regression formulas)

B. Analytic Solution of Scott (Simple Kernel)

$$\frac{dn_i}{dt} = a_{i1}(n_1 - n_{eq1}) + a_{i2}(n_2 - n_{eq2}) + a_{i3}(n_3 - n_{eq3}) \quad (6)$$

$i = 1, 2, 3$

where n_{eqi} is the equilibrium level for component $n_i(t)$.

The solution has the form

$$n_i(t) = n_{eqi} + c_1 v_{i1} e^{\mu_1 t} + c_2 v_{i2} e^{\mu_2 t} \quad , i = 1, 2, 3 \quad (7)$$

where the μ_i 's and v_{ij} 's are determined from the a_{ij} 's in (6) and where the coefficients c_j are determined by the initial conditions. (n_3 can be found from n_1, n_2 since mass is conserved.)

Viewgraph 9.

I. Representation of Breakup

A. Analytic Solution of Feingold

(simple fragment distribution)

B. Parameterization Based on Approx.

Analytic Solution

1. Srivastava (Marshall-Palmer spectrum, fixed no. fragments per breakup)
2. Brown (linearized equations, low resolution)

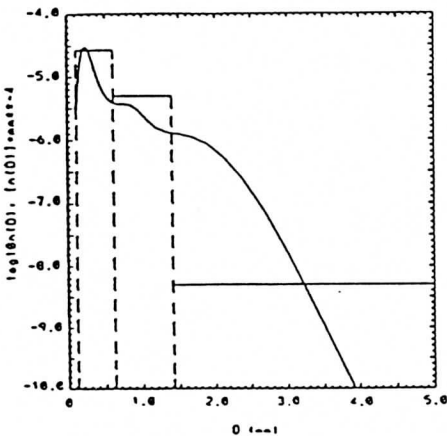
Advantages:

- a) Coalescence and breakup included
- b) "exact" kernel, fragment distribution
- c) any initial distribution
- d) "exact" equilibrium

$$\left(\frac{n(t) - n_{eq}}{n(o) - n_{eq}} \right)_{j(\text{fine grid})} \approx \left(\frac{n(t) - n_{eq}}{n(o) - n_{eq}} \right)_{i(\text{coarse grid})}$$

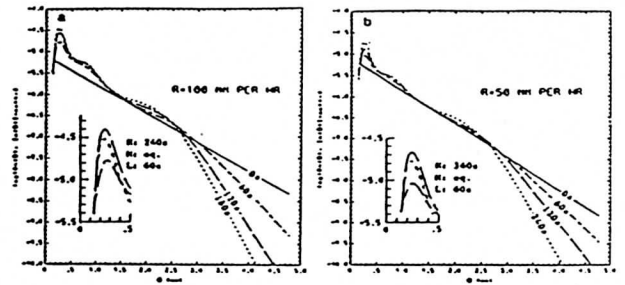
Viewgraph 10.

Viewgraph 7.

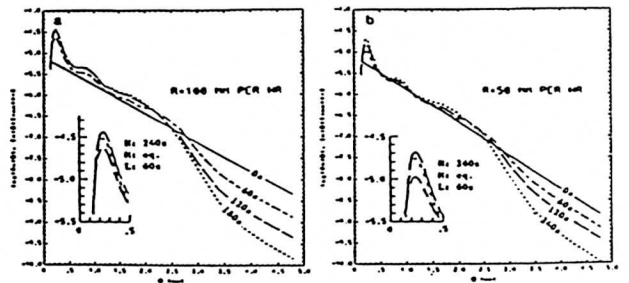


Viewgraph 8.

Detailed Numerical Solution



4-Bin Parameterization



Viewgraph 11.

On The Temperature of The Rain During The Valentines Day Ice Storm

Robert R. Czys
and
Kung-Chyun "KC" Tang

Illinois State Water Survey
Atmospheric Sciences Division
Champaign, Illinois

OVERVIEW

1. Description of Event
2. Drop Temperature Model
3. Model Results

NYG 2-21-90 A1

Governor asks Bush for disaster aid

* Ice Storm

Federal team finds \$3 million in public costs

By J. PHILIP BLOOMER
News-Gazette Staff Writer
and The Associated Press

Gov. James Thompson today asked President Bush to declare Champaign County a major disaster area because of damage from last week's ice storm.

In a letter to the president, Thompson said the storm damage is of such severity and magnitude that an effective response is beyond the capabilities of state and local government.

Thompson cited a federal disaster team's estimate that cleanup and repair costs for public property will exceed \$3 million.

If the president approves Thompson's request, the federal government could provide 75 percent of the recovery dollars with a 25 percent state and local

Federal storm aid estimate



Applicant	Total
Champaign County Forest Preserve District	\$88,100
City of Urbana	549,350
Urbana Park District	87,600
Parkland College	46,700
Village of Mahomet	85,500
Village of Rantoul	718,100
City of Champaign	781,700
Champaign Public Schools	90,000
Champaign-Urbana Sanitary District	10,000
University of Illinois	57,100
Champaign Park District	171,800
Other towns and villages	375,000
Total	\$3,451,950

Source: Federal Emergency Management Agency

■ IP says many to have power back on by tonight, A-3.

THE CHAMPAIGN-URBANA NEWS-GAZETTE

Insurance agencies flooded with claims for storm damages

By RUTHIE DARLING
News-Gazette Staff Writer

Local insurance companies are doing double duty this month, handling numerous, and sometimes hefty, claims from the Valentine's Day ice storm and more recent flooding and high winds.

"It's a long way down the road before we get finished with this thing," said Carolyn Unricker, owner of the Savage-Roth Insurance Agency in Champaign.

She said the agency has been handling 25 claims a day since the Feb. 14 ice storm which cut power to almost 30,000 Illinois Power customers, leaving some in the dark for up to a week.

"You're lucky if you get one claim a day, normally," she said. "But we're catching up now."

hood \$500,000 for his agency and average \$250 per claim.

The agents say most claims stem from flood loss due to a power outage; flood damage to basements because of non-functional sump pumps; and damage to roofs and cars.

Fires occurred in two cases where electrical meters were pulled away from houses by falling limbs.

"A grounded wire allowed current to go into the houses and caused big problems with refrigerators and furnaces," Unricker said. "The (homeowners) were able to get the fire out themselves, but there was damage."

Deary said property loss generally is not a chargeable loss and should not affect insurance premiums.

ter storm, IP still counting costs, weighing rate hike

PHILIP BLOOMER
Staff Writer

CO (the Feb. 14 ice storm) into the millions. Public officials are leaving the possibility of wrapping their expenses into a rate quest.

ements of the utility's price before and after the — including its tree maintenance program and the condition of its power poles and lines



'Could we have done something better? I don't think you can ever say there's not something we could have done better. But I think, in fact I know, we did a good job as a company.'

— Al Anderson, IP service area manager

damage when they set rates. "Using the general model, the idea is one year you have losses and one year you don't have losses, and you hope over the years, the good years balance out the bad years," he said.

THE ICC STAFF investigation under way now is not designed to give the commissioners any direction on the rate hike question. "Right now, the intent of this

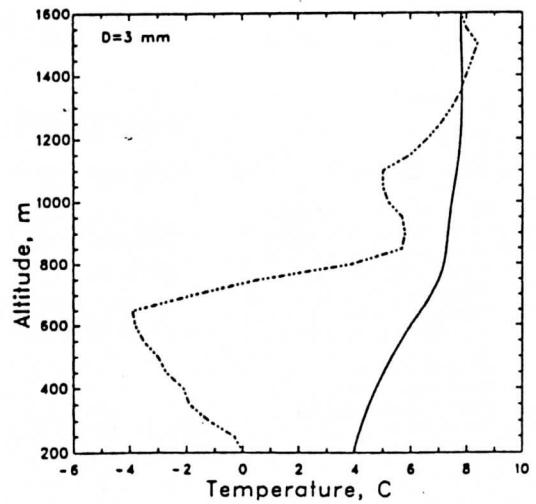
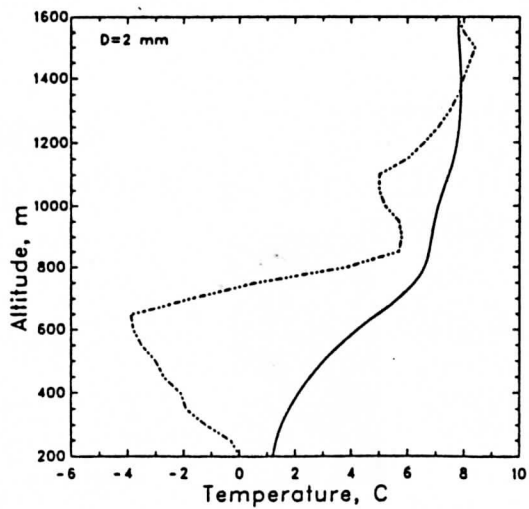
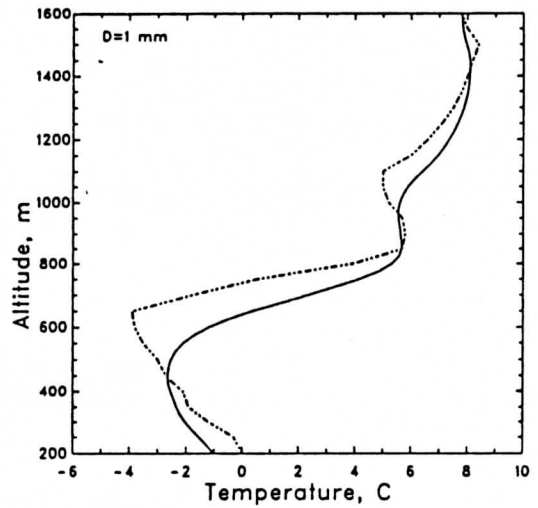
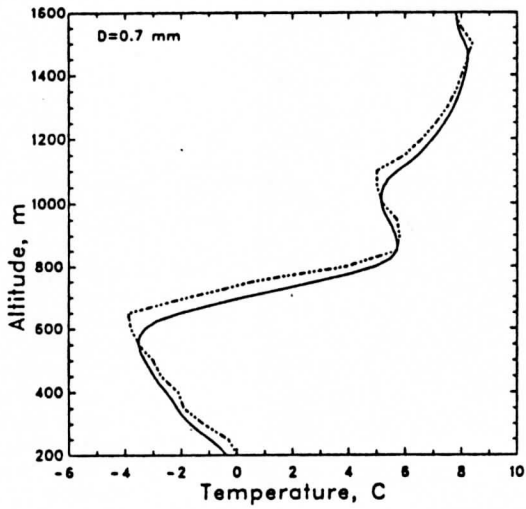
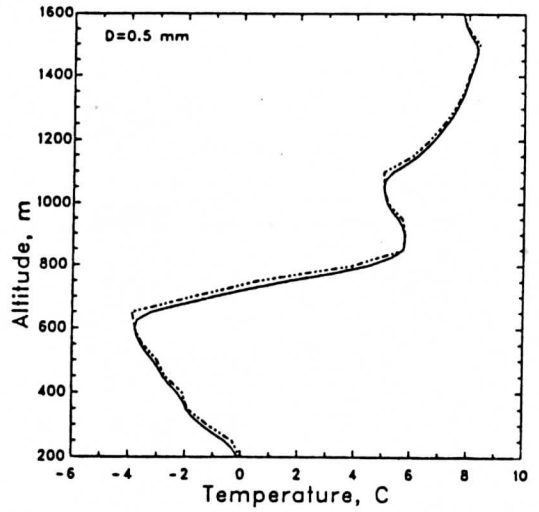
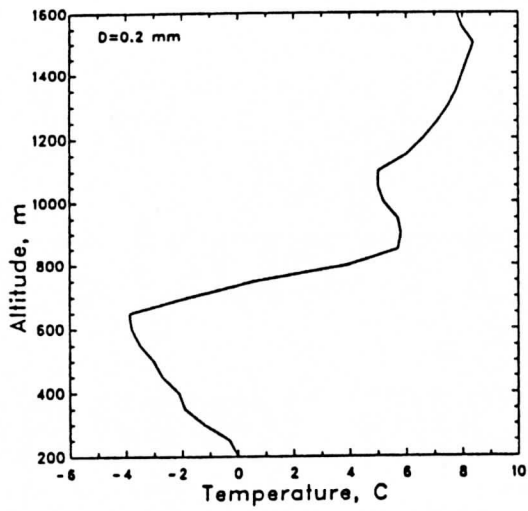
Model Description

$$\frac{\partial T}{\partial t} = \alpha \left[\frac{\partial^2 T}{\partial r^2} + \frac{2}{r} \frac{\partial T}{\partial r} \right]$$

α = thermal diffusivity
of droplet

Assumptions

1. Radially Symmetric
2. No Mass Transfer
3. No Phase Change
4. Ventilation Negligible
5. No Internal Circulation
6. Drop Fall at Terminal Speed
7. No Drop Collection



CASE STUDY

MARCH 23, 1990

COLD FRONTAL PASSAGE
THROUGH COLORADO

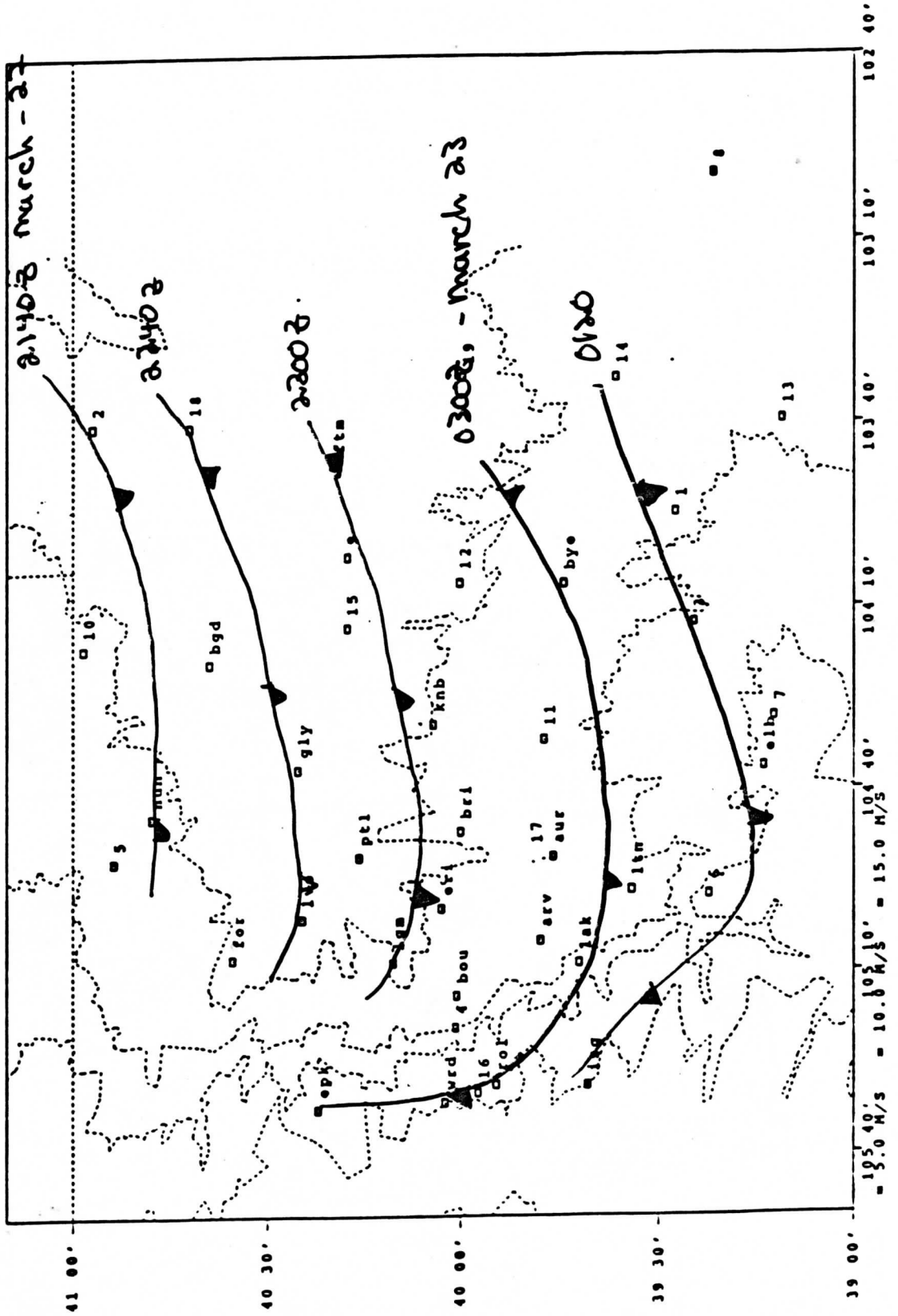
AN ICING EVENT

OUTLINE

- 1) SYNOPTIC AND MESOSCALE OVERVIEW
- 2) VERTICAL STRUCTURE OF FRONT
- 3) RUDIMENTARY ANALYSIS
- 4) FUTURE RESEARCH

mesoscale cold frontal passage through WISP Domain.
Note the difference between the synoptic and mesoscale analysis.

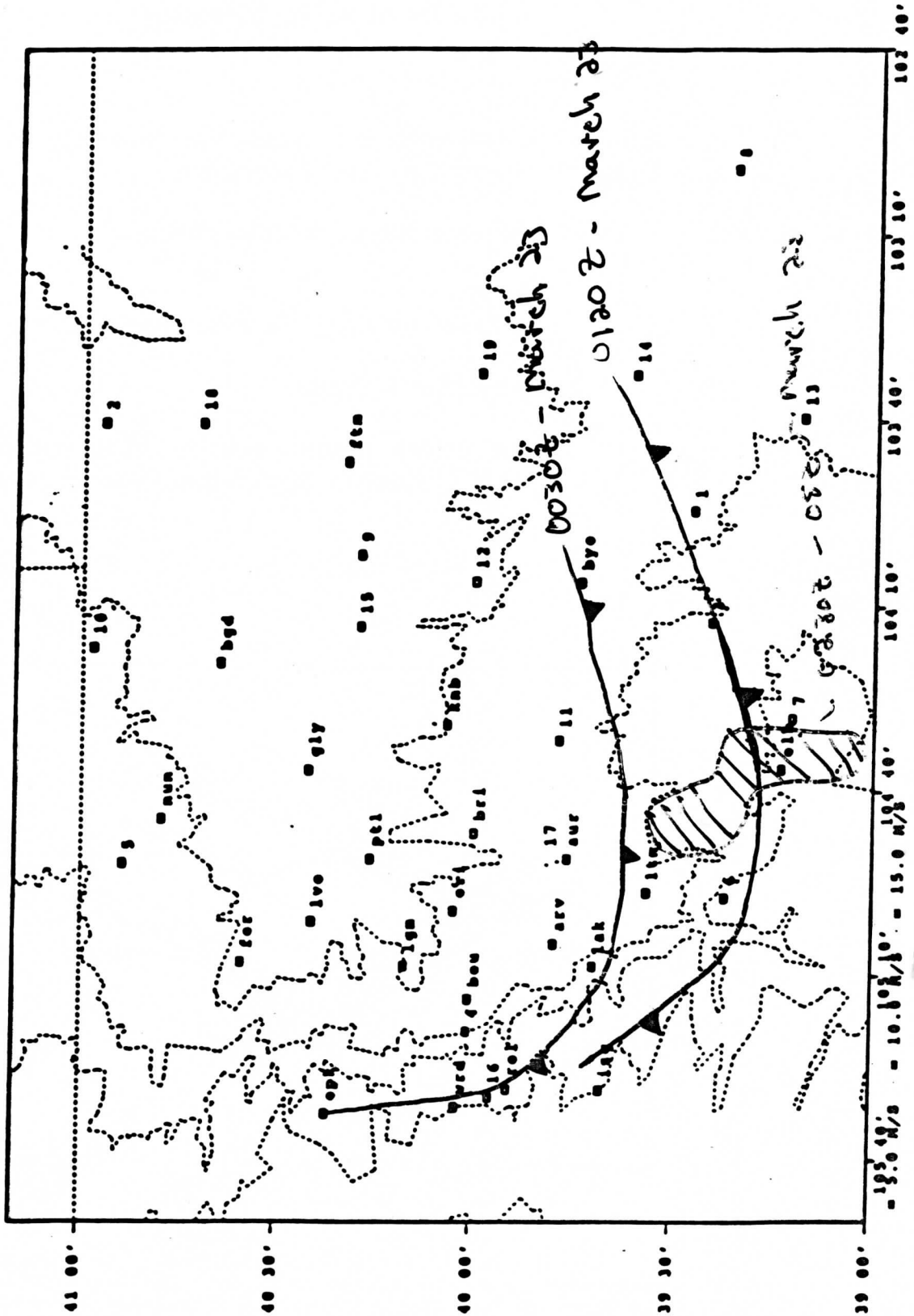
PAM and PROFS mesonet sites for WISP-1990



ARROWS COLOR CODED BY MAXIMUM WIND SPEED
0.00 6.67 11.33 20.00 26.67 33.33 (M/S) MISSING

Region of super cooled liquid water. Found in a temperature range of -3.0 - -7.5°C , and pressure range of 787 - 712 mb

PAM and PROFS mesonet sites for WISBP-1990



Arrows color coded by MAXIMUM WIND SPEED

DO WE HAVE GOOD ROLL MODELS?

David A. R. Kristovich

Using observations to test models (parameters)
Using models to interpret observations

1. Roll characteristics (Flow fields)

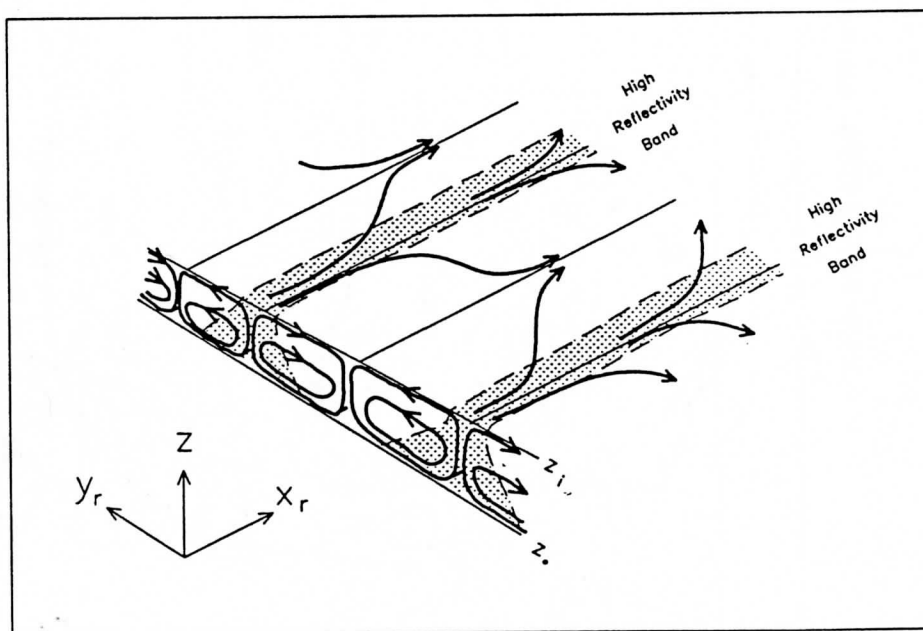
Roll-mean

Convection along the rolls (statistical)

2. Convective Regimes

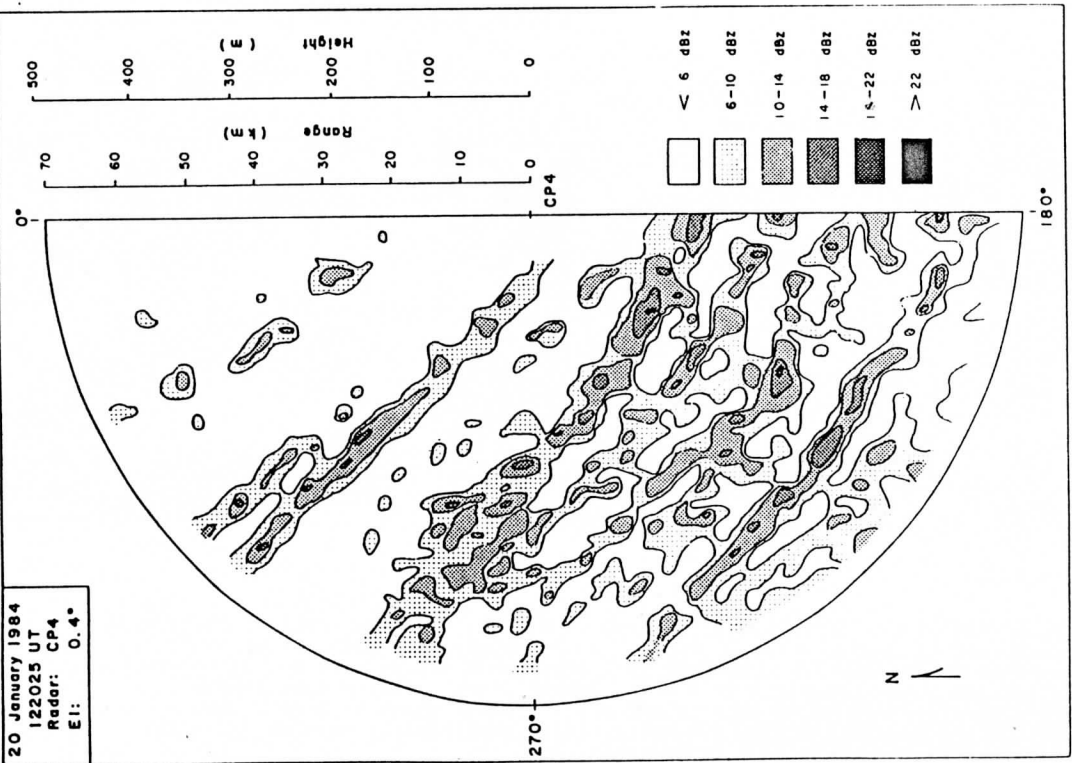
Do models produce rolls in similar conditions?

Roll Formation Mechanisms (obs see results)

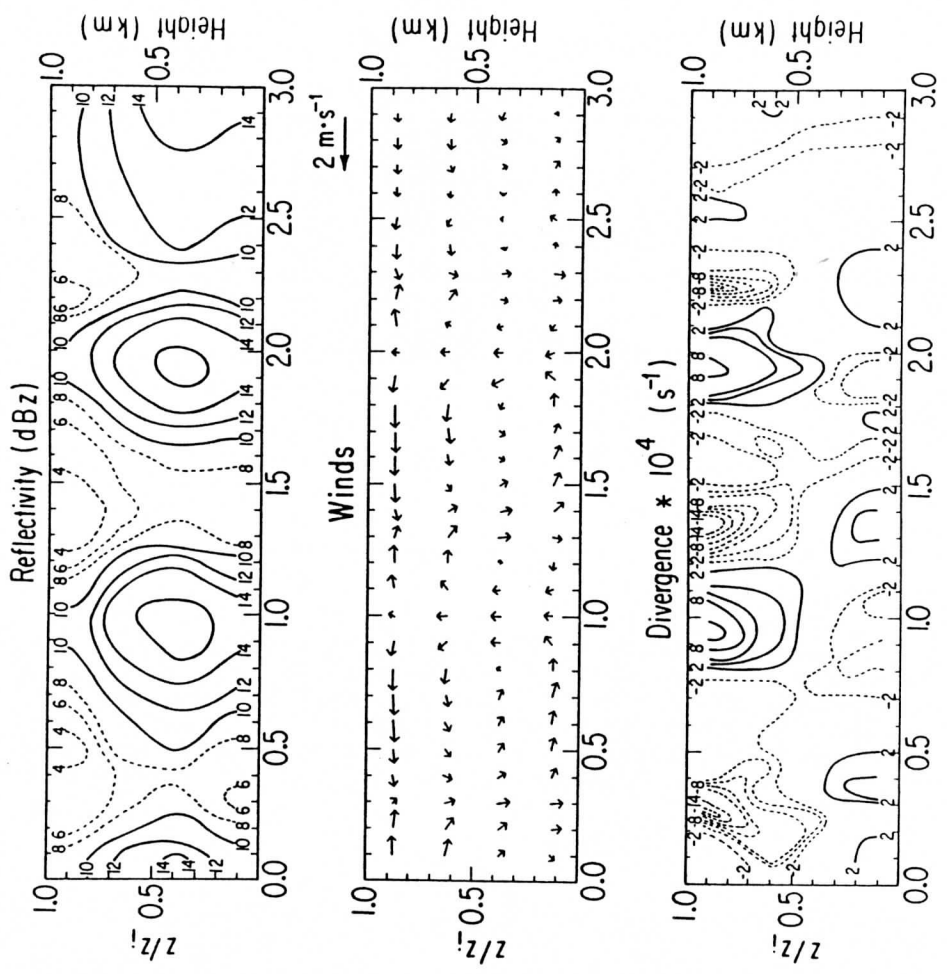


Schematic of roll circulations. The boundary layer mean wind is in the direction of x_r . The boundary layer top is shown as z_i . The high-reflectivity bands are shaded.

20 January 1984
 122025 UT
 Radar: CP4
 EI: 0.4°



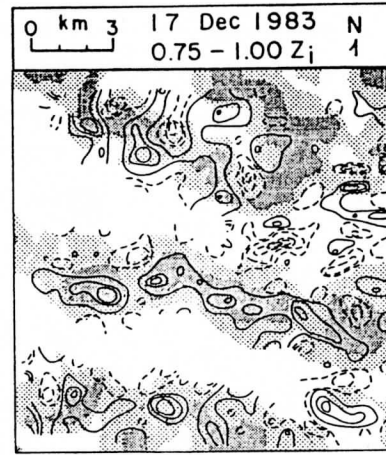
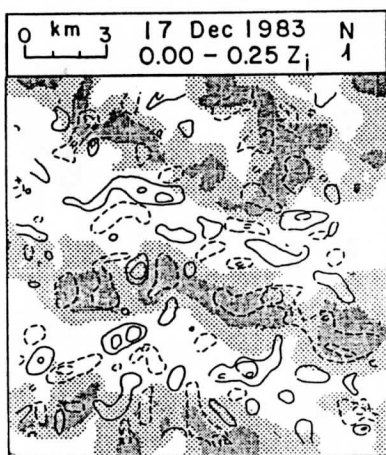
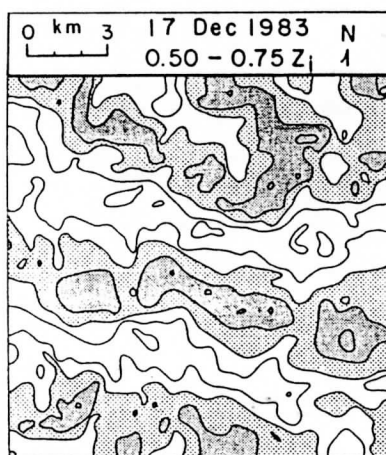
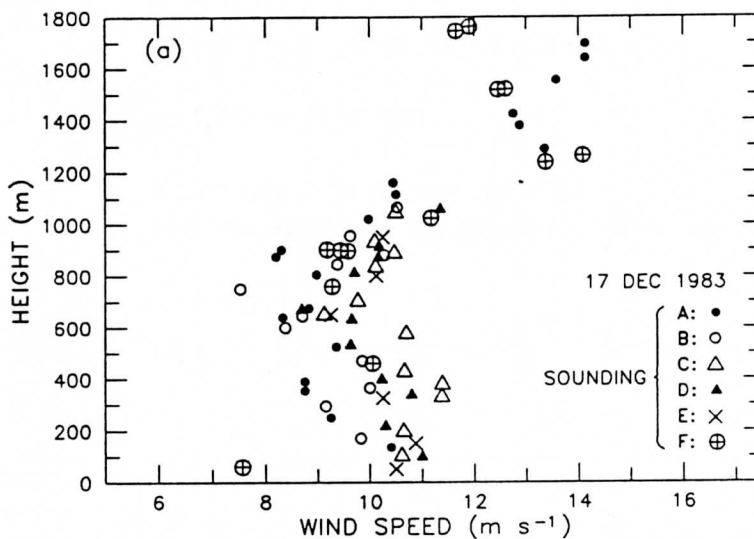
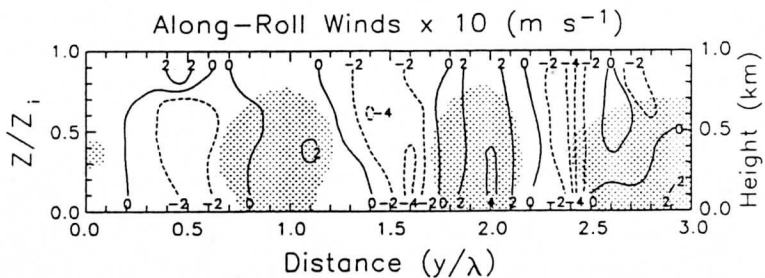
17 December 1983



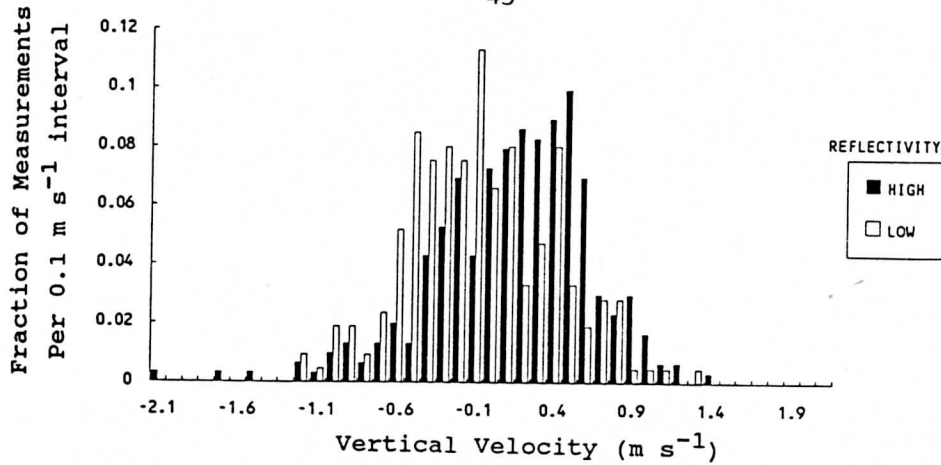
Roll-Relative Distance

Map of southern Lake Michigan showing a few cities and airports in the region. The locations of NCAR radars CP3 and CP4 during Project Lake Snow are shown.

NNE 17 December 1983, 1541 UT SSW



Plan view of (a) reflectivity at 0.50 to 0.75 Z_i , (b) low-level (0.00 to 0.25 Z_i) divergence, and (c) upper-level (0.75 to 1.00 Z_i) divergence measured by dual-Doppler radars on 17 Dec 1983 at 1541-1543 UT. Divergence values were calculated for 1 km^2 areas and contoured every $1 \times 10^{-3} \text{ s}^{-1}$. Dashed areas indicate convergence. Reflectivity values are contoured every 5 dBZ from a lowest value of 0 dBZ, with darkest shadings for high reflectivity. Reflectivity shadings are also shown in (b) and (c). Each box represents a $14 \times 14 \text{ km}$ area.



Frequency distribution of vertical velocities derived from radar-measured divergence values for each 1 km² area in a 196 km² sample region. Solid columns represent vertical velocities in high-reflectivity bands and open columns represent those in low-reflectivity regions. Data were taken on 17 Dec 1983 at 1541-1543 UT.

**Percent of Km-Scale Mass Flux
Accounted for by Rolls**

	17 Dec	18 Dec	29 Dec	20 Jan
Roll Up/Total Up High-Refl Bands	27.6	18.2	36.0	22.3
Roll Dn/Total Dn Low-Refl Bands	17.7	43.5	31.0	30.5
Mean	22.7	30.9	33.5	26.4

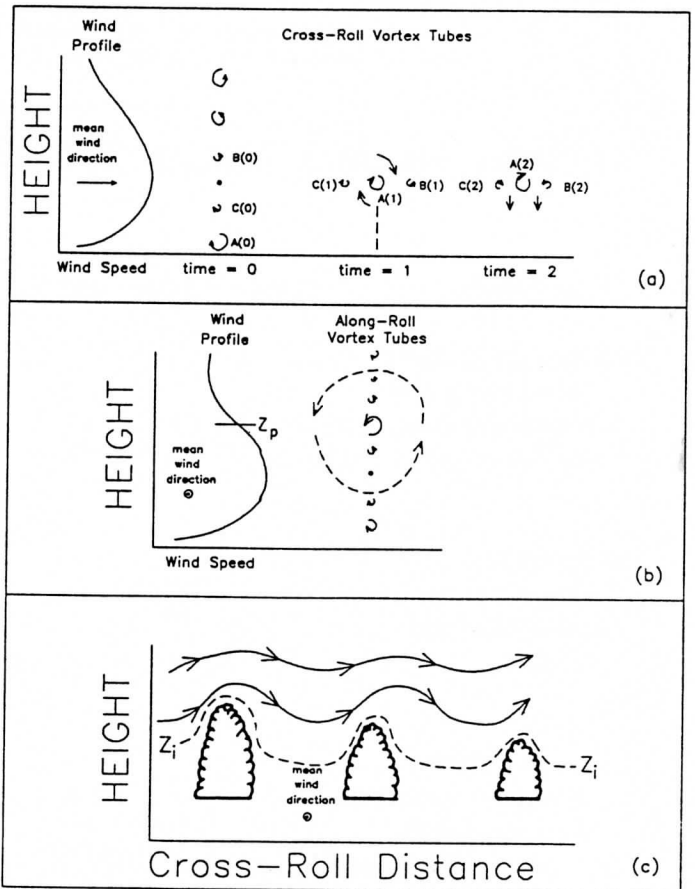
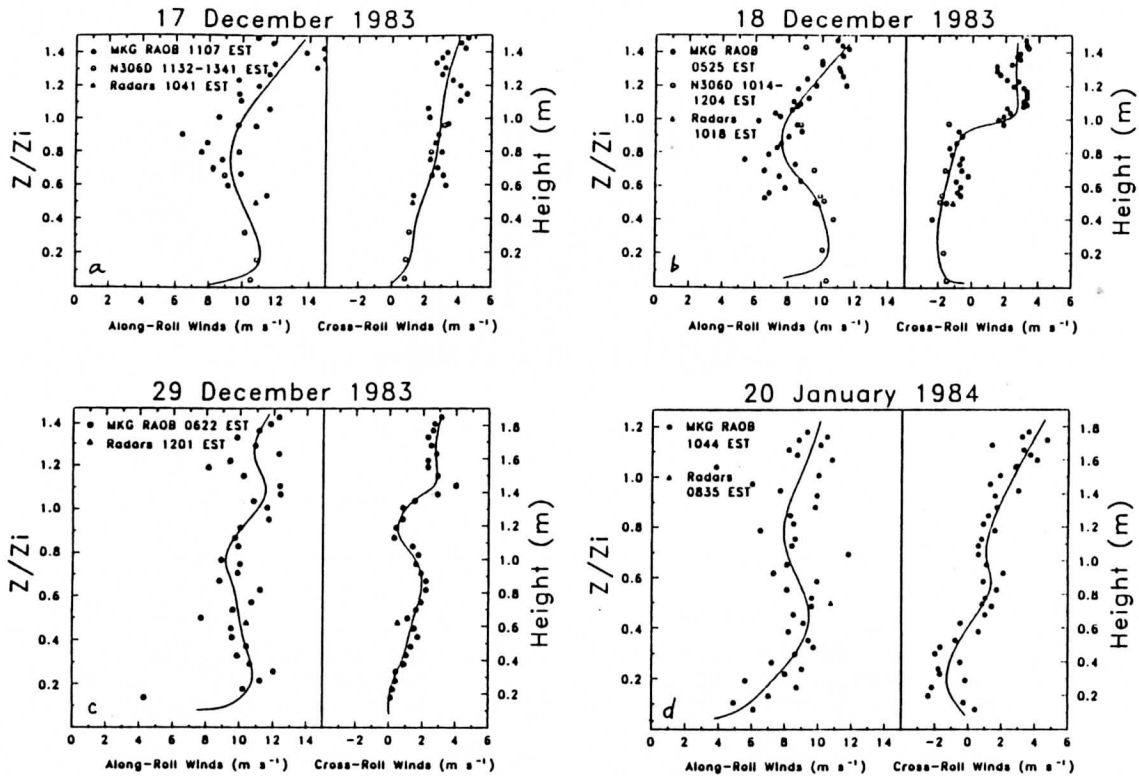


Illustration of three roll formation theories proposed by (a) Kuettner (1959, 1971), (b) Brown (1970; 1972) and (c) Clark et al. (1986). Rotation arrows in (a) and (b) denote direction and magnitude of vortex tubes. Larger rotation arrows denote larger magnitudes. The mean boundary layer wind direction is from left to right in (a) and into the page in (b).



Profiles of along- (U_r) and cross-roll (V_r) components of the horizontal wind speed on (a) 17 Dec, (b) 18 Dec, and (c) 29 Dec 1983 and (d) 20 Jan 1984. Height is normalized by boundary-layer depth on the left side of each plot. These data were taken by balloon soundings over Muskegon, Michigan, dual-Doppler radars and aircraft.

Criteria for Roll Forcing Mechanisms

PRIMARY FINDINGS

Author/Criteria	17 Dec	18 Dec	29 Dec	20 Jan
Kuettner (1959, 1971)				
Curved Along-Roll Wind Profile Over 10 ⁻⁷ cm ⁻¹ s ⁻¹	Y	Y	Y	Y
BL: 10 ⁻⁷		10 ⁻⁸	10 ⁻⁸	10 ⁻⁸
LL: 10 ⁻⁶		10 ⁻⁶	10 ⁻⁶	10 ⁻⁷
Brown (1972)				
Inflection Pt. in Cross-Roll Wind Profile	N	N	N	Y
Clark, et al. (1986)				
Gravity waves above BL	N	Y	N	N
Shear at top of BL 90° to roll orientation	-17°	-77°	-40°	-52°

CONVECTION ORGANIZED INTO LINES BY LOW-LEVEL SHEAR

"ROLL-MEAN" FLOW FIELDS INDICATE EXISTENCE OF ROLLS

ALONG-ROLL COMPONENT OF THE WIND VARIATIONS DUE TO VERTICAL ADVECTION OF HORIZONTAL WIND PROFILE

CONVECTION ALONG ROLLS FOUND TO BE

- PERSISTENT
- OCCURS IN BROAD BAND (+/- 1 KM) NEAR ROLL UPDRAFT
- GREATLY MODIFIES ROLL FLOW FIELD

MASS FLUX DUE TO ROLL CIRCULATIONS IS A SMALL FRACTION OF THAT FROM OTHER KM-SCALE CIRCULATIONS

Regarding the Behavior of Merging Radar Echo Cores

by

Nancy E. Westcott

Clouds and Precipitation Office

Illinois State Water Survey

KEY POINTS

1. Merger of isolated cores is only one way in which storms become multicelled and expand in area.

2. 90 echo core mergers occurring during 2 convective periods in central Illinois during the summer of 1986 were examined.

3. a. 50-70 % of the cores which merged, grew in area after merger;

b. 60-80 % of the cores growing in area before merger continued to grow in area after merger.

c. 65-95 % of the cores growing in area following merger were growing in area prior to merger.

Thus, if a core was growing after merger, it was very likely that it was growing prior to merger.

4. Generally, it was found that when the younger core 2 was growing after merger, it was younger, smaller, and had a more elevated max reflectivity core and a higher echo base than did those not growing after merger.

5. One or both of the reflectivity cores in the merger pair were expanding in area at the time of merger.

6. Merger of the reflectivity cores occurred by horizontal expansion of area of the cores. In only 10-15 % of the cases did differential core motion and/or a new core bridging 2 older cores, contribute to merging of the cores.

7. The bridges joining the merging cores were deeper by being both considerably lower and somewhat taller than first echoes observed on the same day. This might result from moisture laden downdraft air mixing into the air in the area of bridge formation, enhancing the amount of low level water vapor available for cloud particle growth. This also may occur from the horizontal expansion through a deep layer of the two cores, where at least one was generally older than a first echo.

	25 July 1986		26 August 1986	
	Core 1	Core 2	Core 1	Core 2
Max Reflectivity	22	58	48	62
Area ≥ 20 dBZ	48	48	67	65
Area ≥ 35 dBZ	62	52	71	59
Height	33	46	29	34

	25 July 1986		26 August 1986	
	Core 1	Core 2	Core 1	Core 2
Max Reflectivity	27	71	56	69
Area ≥ 20 dBZ	60	62	79	66
Area ≥ 35 dBZ	82	69	84	67
Height	17	50	30	46

	25 July 1986		26 August 1986	
	Core 1	Core 2	Core 1	Core 2
Max Reflectivity	60	86	72	81
Area ≥ 20 dBZ	67	91	88	86
Area ≥ 35 dBZ	69	92	91	85
Height	13	73	33	48

Table 4a. Characteristics at the time of merger for the echo core on 25 July 1986, grouped by whether or not echo 2 was growing.

	Growing	Not Growing
Sample Size	11	8
Bridge:		
Maximum Height (km)	8.5	10.5
Max Z Height (km)	5.5	6.5
Minimum Height (km)	3.5	2.5
Depth (km)	4.0	5.5
Max Reflectivity (dBZ)	25.0	25.0
Core 1:		
Age at Merger (min)	15	30
Area of dBZ ≥ 35 (km ²)	22	33
Core Top Height (km)	11.0	11.5
Core Max Z Height (km)	6.5	6.0
Core Base Height (km)	1.5	1.5
Max Reflectivity (dBZ)	45.0	45.5
Core 2:		
Age at Merger (min)	5	15
Area of dBZ ≥ 35 (km ²)	2	16
Core Top Height (km)	10.5	8.5
Core Max Z Height (km)	6.5	3.5
Core Base Height (km)	2.5	1.5
Max Reflectivity (dBZ)	37.5	41.5

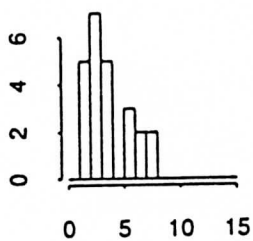
Table 4b. Characteristics at the time of merger for the echo cores on 26 August 1986, grouped by whether echo 2 was growing.

	Growing	Not Growing
Sample Size	36	15
Bridge:		
Maximum Height (km)	5.5	6.0
Max Z Height (km)	4.5	4.5
Minimum Height (km)	2.5	1.5
Depth (km)	3.0	4.0
Max Reflectivity (dBZ)	27.5	22.5
Core 1:		
Age at Merger (min)	10	21
Area of dBZ ≥ 35 (km ²)	22	38
Core Top Height (km)	8.0	8.5
Core Max Z Height (km)	3.5	3.5
Core Base Height (km)	1.5	1.5
Max Reflectivity (dBZ)	51.3	50.0
Core 2:		
Age at Merger (min)	7	11
Area of dBZ ≥ 35 (km ²)	8	9
Core Top Height (km)	6.5	6.5
Core Max Z Height (km)	4.5	2.5
Core Base Height (km)	1.5	1.0
Max Reflectivity (dBZ)	45.0	43.8

Table 5. Bridge and first echo median characteristics.				
	25 July 1986		26 August 1986	
	First Echo	Bridge	First Echo	Bridge
Sample size	30	24	79	66
Max dBZ	26.9	25.0	28.7	27.5
Echo Top (km)	7.5	8.5	5.5	5.5
Max dBZ ht.(km)	6.5	6.5	5.5	4.5
Echo Base (km)	4.5	3.0	4.5	1.5
Depth (km)	3.0	5.0	1.0	4.0
Freezing Level (km)	4.5		4.3	
Cloud Base (km)	2.0		1.0	

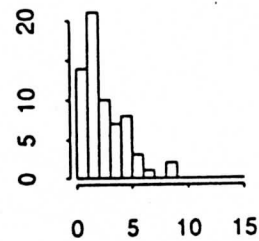
Bridge and First Echo Base Heights

7/25/86 Bridge median= 3



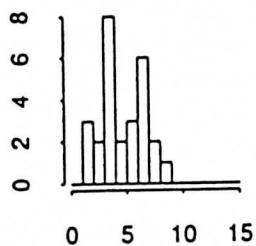
Bridge Base Height (km)

8/26/86 Bridge median= 1.5



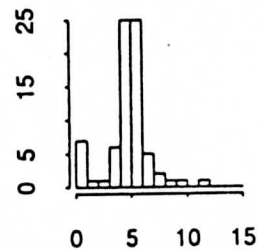
Bridge Base Height (km)

7/25/86 Merging FE median= 4.5



First Echo Base (km)

8/26/86 Merging FE median= 4.5



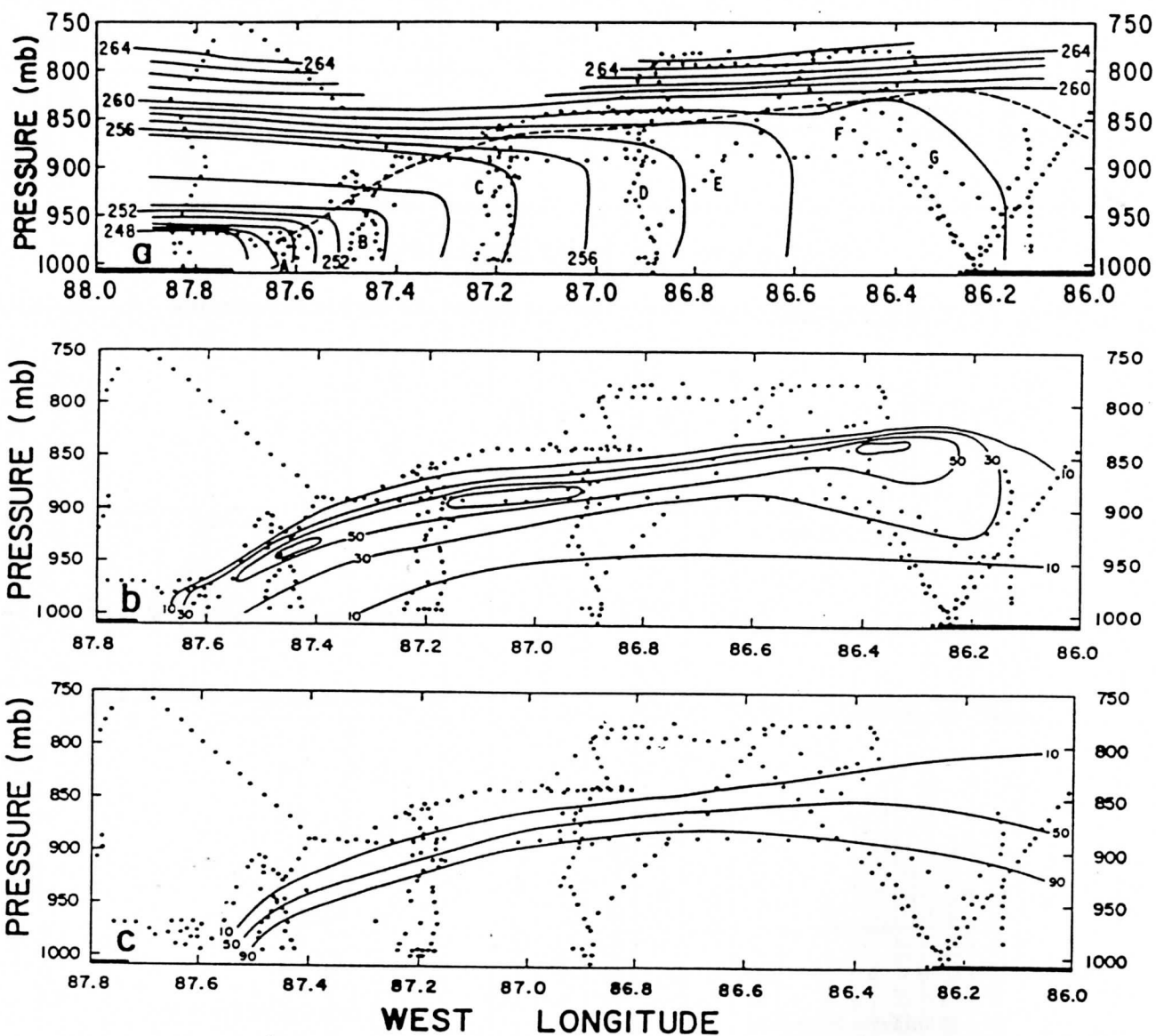
First Echo Base (km)

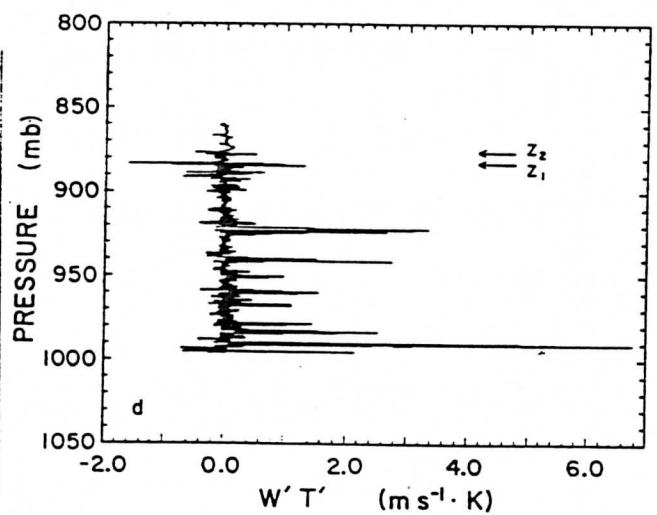
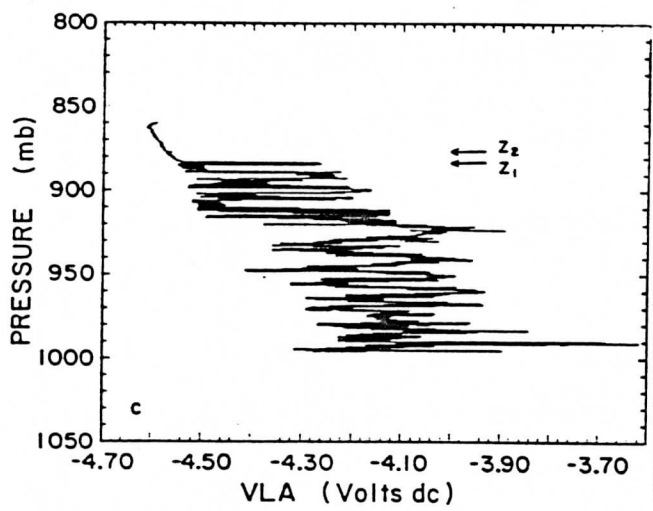
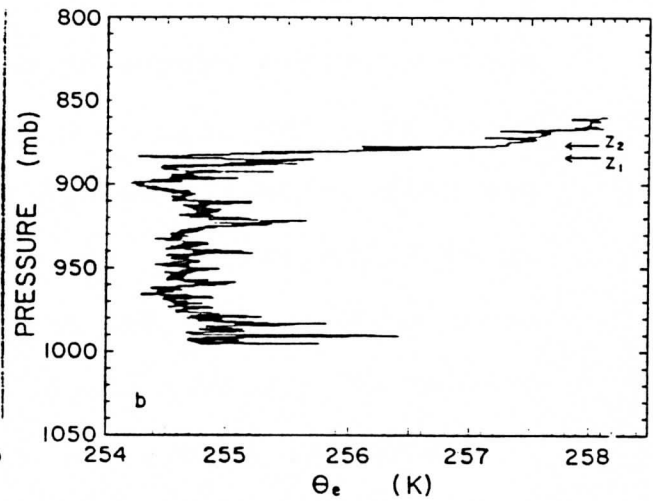
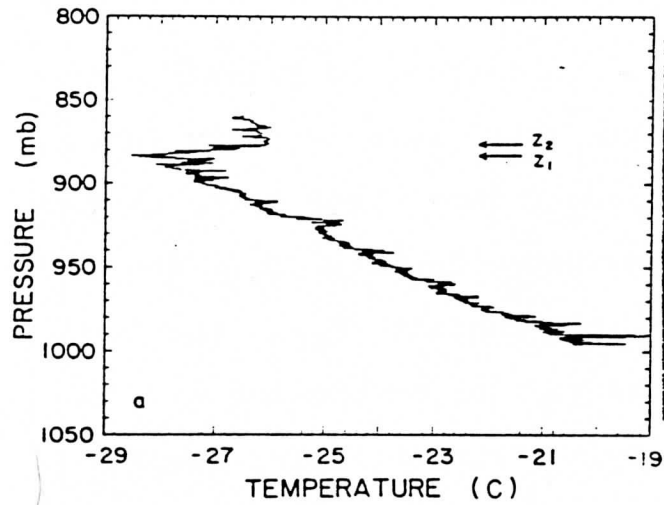
MACAP 91

Heat and Water Budget for a
Lake-Effect Snow Storm

R. Braham, Jr., and S. Chang

Adapted from Chang and Braham, 1991: Observational
Study of a Convective Boundary Layer over Lake Michigan. J.
Atmos. Sci., 48, xx-xx (accepted).





6. WATER BUDGET

For a two-dimensional analysis, the conservation of the total water and the conventional Reynolds averaging yield:

$$\frac{\partial \bar{Q}}{\partial t} + \frac{\partial}{\partial x} \bar{Q} \bar{u} + \frac{\partial}{\partial z} \bar{Q} \bar{w} = - \frac{\partial}{\partial x} \overline{Q'u'} - \frac{\partial}{\partial z} \overline{Q'w'} \quad (4)$$

where overbars represent mean quantities and primes deviations from the means. Q is the total water density (mass per unit-volume). We can divide Q into three parts as done by Nicholls (1984): the vapor water density (Q_V), the cloud water density (Q_C) and snow water density (Q_S). The integration of (1) from the bottom ($z = 0$) to the top ($z = z_i$) of a boundary layer, and applying Leibnitz rule, results in

$$\frac{\partial}{\partial x} \int_0^{z_i} \bar{Q} \bar{u} dz = \underbrace{\bar{Q}(z_i)w_e}_{<2>} + \underbrace{\overline{Q'u'}(0)}_{<3>} - \underbrace{\overline{Q'u'}(z_i)}_{<4>} + \varepsilon \quad (5)$$

<1>

where ε absorbs all the terms which are considered to be small;

$$\varepsilon = \overline{Q'u'}(z_i) \frac{\partial z_i}{\partial x} - \frac{\partial}{\partial x} \int_0^{z_i} \overline{Q'u'} dz - \frac{\partial}{\partial t} \int_0^{z_i} \bar{Q} dz. \quad (6)$$

Table 3. Values of various terms in the total water budget, 20 Jan 1984 lake-snow storm

Terms	Fetch avg.						Units
Fetch (x)	9.7	33.8	51.5	81.5	116.7		km
CIBL depth	259	641	1009	1186	1359		m
Vert. integral horiz. flux	1.23	3.71	5.40	7.83	10.60		kg m ⁻¹ s ⁻¹
Avg. rate of change, horiz. flux <1> x 10 ⁶	102.9	95.5	81.1	78.6	87.6		kg m ⁻² s ⁻¹
Entrain. flux <2> x 10 ⁶	55.7	37.0	19.9	13.7	12.3		kg m ⁻² s ⁻¹
Average x 10 ⁶	46.3	28.4	16.8	13.0	24.1		kg m ⁻² s ⁻¹
Sfc. Evaporation <3a> x 10 ⁶	112.5	107.6	108.5	89.4	88.0		kg m ⁻² s ⁻¹
Sfc. Snowfall <3c> x 10 ⁶	0	-3.2	-12.2	-12.5	-12.3		kg m ⁻² s ⁻¹
Avg. sfc. flux <3> x 10 ⁶	108.5	100.4	86.6	76.3	90.4		kg m ⁻² s ⁻¹
Eddy flux CI., top							
vapor							
<4a> x 10 ⁶	42	34	12	12	12		kg m ⁻² s ⁻¹
liquid							
<4b> x 10 ⁶	4	1	1	3	1		kg m ⁻² s ⁻¹
Avg. eddy flux CIBL top <4> x 10 ⁶	40.5	24.0	14.0	14.0	21.6		kg m ⁻² s ⁻¹
Residual <ε> x 10 ⁶	-11.4	-9.3	-8.3	3.3	-5.3		kg m ⁻² s ⁻¹

$$\begin{aligned}
z_i \left[\frac{\partial \bar{\theta}_e}{\partial t} + \bar{u} \frac{\partial \bar{\theta}_e}{\partial x} \right] &= \left[\overline{w'\theta'_e} \right]_0 - \left[\overline{w'\theta'_e} \right]_{z_i} \\
&+ \left[\frac{R}{\rho_a C_p} \right]_0 - \left[\frac{R}{\rho_a C_p} \right]_{z_i} \quad (12) \\
&- \int_0^{z_i} \frac{\partial \overline{u'\theta'_e}}{\partial x} dz.
\end{aligned}$$

It is obvious from (11) that

$$\overline{w'\theta'_e} = \overline{w'\theta'} + C_1 \overline{w'q_v'} \quad (13)$$

and

$$\rho_a C_p \overline{w'\theta'_e} = \rho_a C_p \overline{w'\theta'} + \rho_a L \overline{w'q_v'}. \quad (14)$$

Hence, the equivalent potential temperature flux consists of potential temperature flux (correspondingly, sensible heat flux, $\rho_a C_p \overline{w'\theta'}$) and water vapor flux (latent heat flux $\rho_a L \overline{w'q'}$). The third and fourth terms on the right side of (12) are the net radiative flux at $z = 0$ and $z = z_i$. The simple arrangement of (12) gives us the following form for the mean mixed layer heat budget in terms of θ_e :

$$\begin{aligned}
\bar{u} \frac{\partial \bar{\theta}_e}{\partial x} &= z_i^{-1} \left[\left[\overline{w'\theta'_e} \right]_0 - \left[\overline{w'\theta'_e} \right]_{z_i} \right] \\
&\quad \langle 1 \rangle \qquad \qquad \qquad \langle 2 \rangle \\
&+ z_i^{-1} \left[\left[\frac{R}{\rho_a C_p} \right]_0 - \left[\frac{R}{\rho_a C_p} \right]_{z_i} \right] + \epsilon_1 \\
&\qquad \qquad \qquad \langle 3 \rangle \qquad \qquad \qquad \langle 4 \rangle
\end{aligned} \quad (15)$$

Table 4. Values of various terms in the total heat budget, 20 Jan 1984 lake-snow storm.

Terms	Fetch	Units
Fetch: (x)	9.7	33.8
CIBL Depth (z_i)	259	641
Air density at z_i	1.375	1.300
Mean Equiv. Pot. Temp.	249.1	252.9
Mean Wind Speed	11.7	11.5
Avg. advec. warming rate $\langle 1 \rangle \times 10^3$	1.83	1.07
Eddy Flux, Sfc.	0.42	0.32
Sensible heat.	384	397
Total heat	666	666
Eddy Flux, Top	0.32	0.81
Sensible heat	-55	-52
Total heat.	50	33
Avg. eddy flux div. $\langle 2 \rangle \times 10^3$	1.32	0.63
Radiation flux	0.41	0.29
Surface	-80	-60
CIBL Top	-150	-180
Avg. Rad. flux div. $\langle 3 \rangle \times 10^3$	0.16	0.11
Residual $\langle 4 \rangle \times 10^3$	0.35	0.32

BL heating 698

An Indirect Climatology of Midwestern Cloudiness

Mary Schoen Petersen
Illinois State Water Survey

Implementation of A Semi-Physical Model for Examining Solar Radiation (SR) in the Midwest

Masters Thesis

Mary Schoen Petersen

(Kenneth E. Kunkel and Peter J. Lamb)

Semi-Physical SR Model:

$$I = I_o (\cos Z) T_R T_g T_w T_a T_c$$

I = solar radiation received at the earth's surface

I_o = extraterrestrial flux density at the top of the atmosphere

Z = zenith angle

T_i = transmission coefficients after

- R Rayleigh scattering
- g absorption by permanent gases
- w absorption by water vapor
- a absorption and scattering by aerosols
- c absorption and scattering by clouds

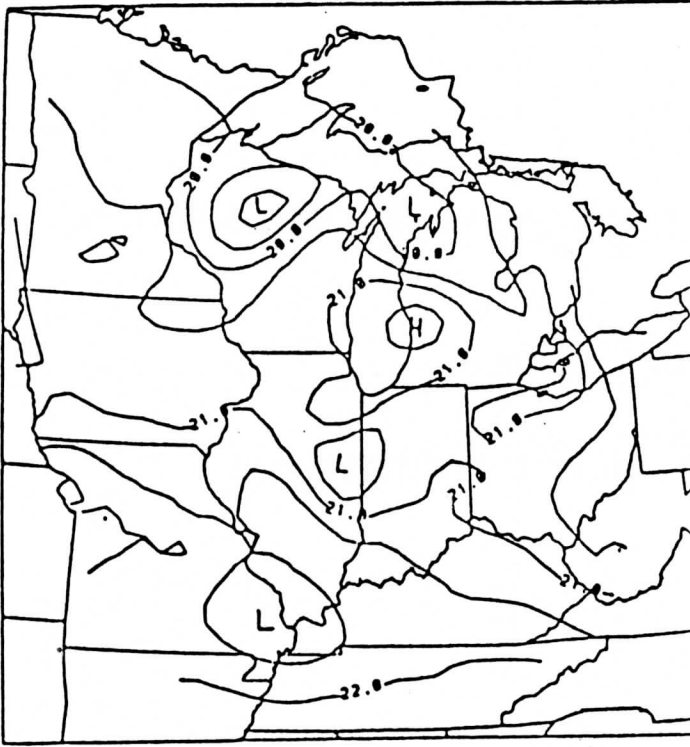
Model Input Data

time of day (hour)
 day of year
 latitude - longitude
 surface pressure
 dew point temperature
 cloud height and fractional coverage
 snow cover

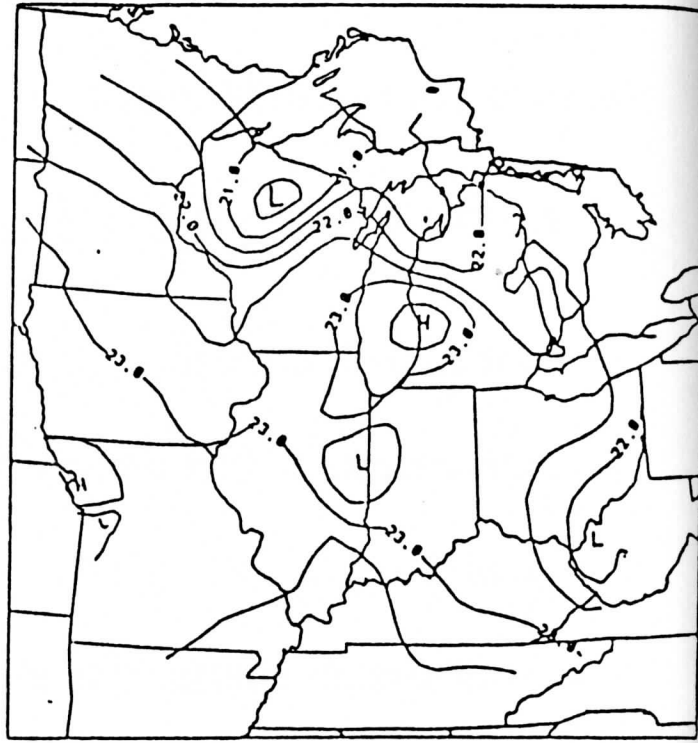
Period-of-Record (1948-1987) 53 stations in Midwest

Model results within 10% of measured SR data

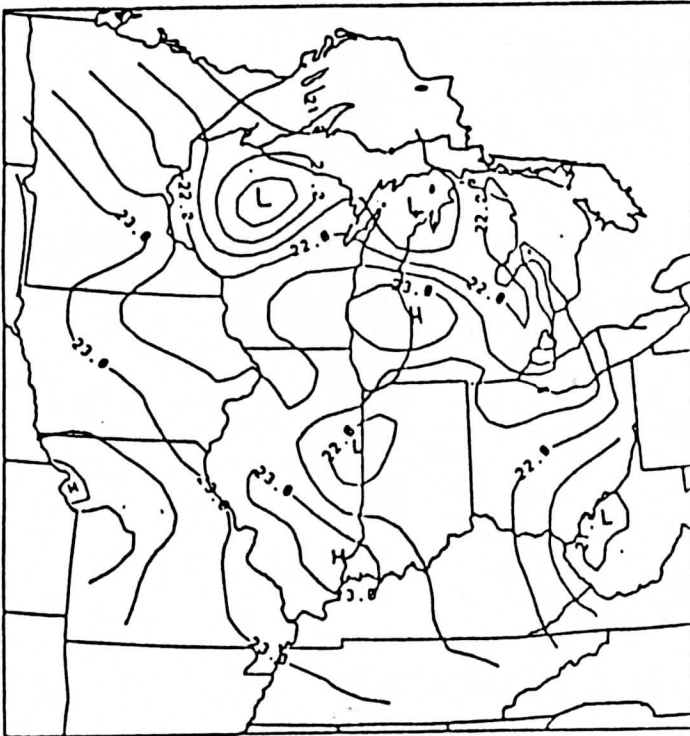
MAY



JUNE



JULY



AUGUST

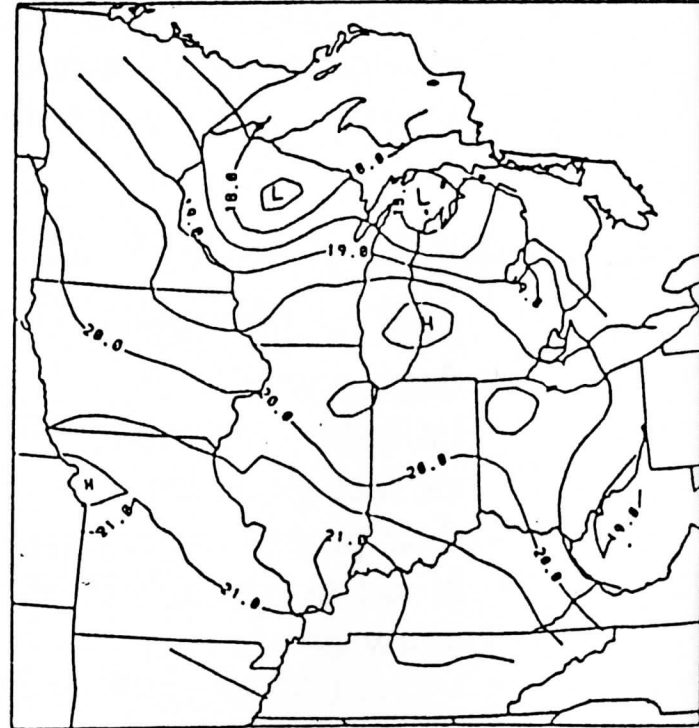


Fig. 4.2. As in Fig. 4.1, but for May, June, July, and August.

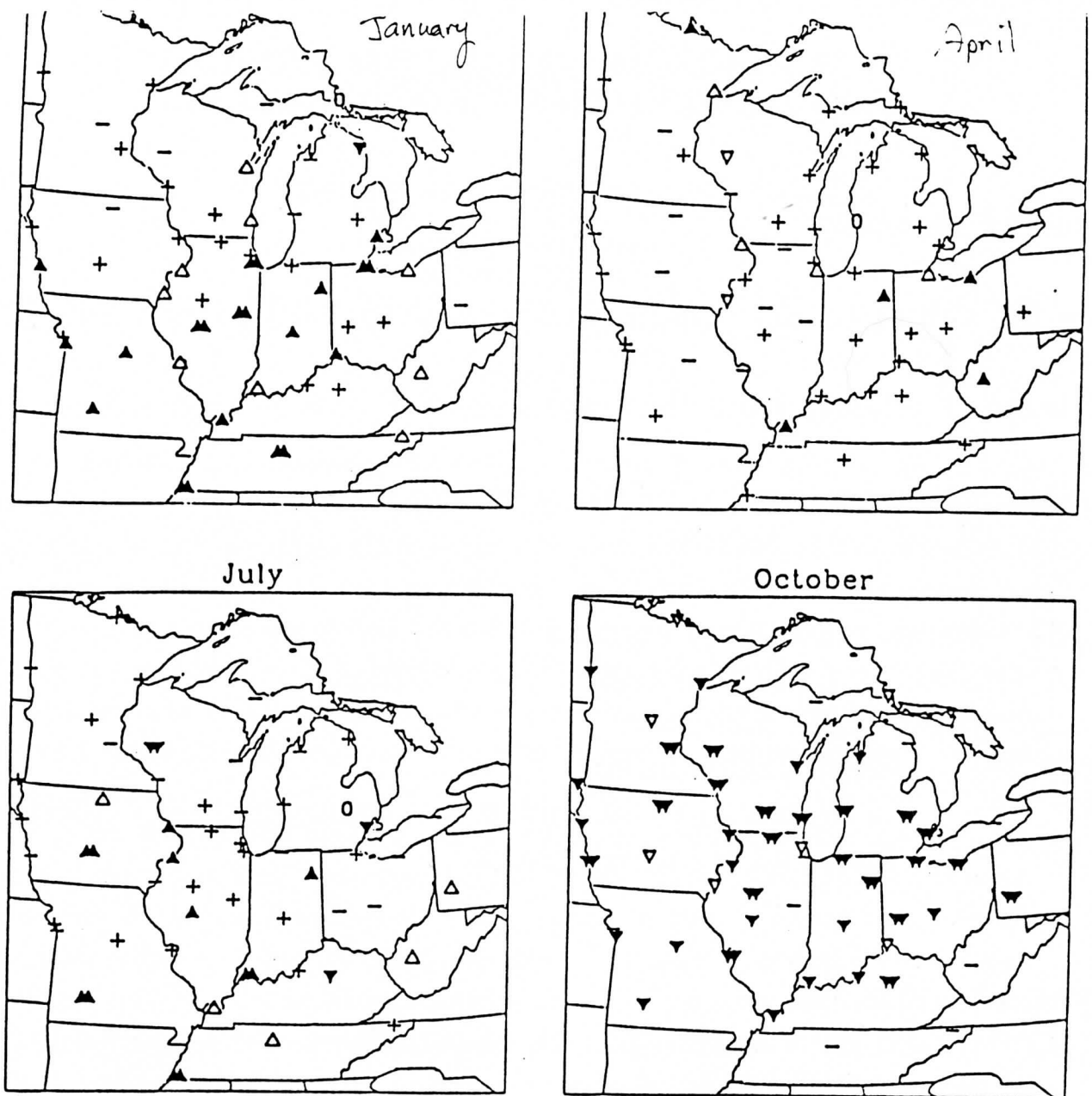


Fig. 4.8. Spatial coherence of SR trends for 1948-1987 for January, April, July, and October months. Relatively insignificant (<90%) positive and negative trends are shown with a + and -, respectively; significant (90-95%) positive and negative trends display a Δ and ▽, respectively; and highly significant (>95%) positive and negative trends are shown as ▲ and ▼, respectively. Double solid triangles indicate significance at the >99% confidence level. No trend is signified by a 0.

SUMMARY

SR model successful

Daily SR values for 53 stations in Midwest for ~40 years (1948-1987)

Can infer cloudiness from SR results since T_c has a large effect in model

Monthly SR means across the Midwest show:

- 1) Northward decrease
- 2) NW-SE orientation of isopleths
- 3) Large gradient in October
- 4) Smooth pattern in Fall to early Winter
- 5) Meso-scale features

Great Lakes effect

N Wisconsin - Michigan low values Spring - Summer

Kansas City urban effect

40-year trends show:

- 1) Strikingly coherent pattern of significant decreasing SR (increasing cloudiness) in October
- 2) Mostly positive SR tendencies (decreasing cloudiness) for the other mid-season months

CLLOUD DYNAMICAL AND MICROPHYSICAL PROCESSES IN SIMULATED CCOPE STORM

Daniel E. Johnson and Pao K. Wang
Department of Meteorology
University of Wisconsin
Madison, WI 53706

ABSTRACT

The Wisconsin Dynamical/Microphysical Model (WISCDYMM) is used to simulate the dynamic, kinematic, microphysical, and precipitation processes operating in an intense Northern High Plains supercell storm that occurred on 2 August 1981 in southeastern Montana. The observed supercell was highly glaciated and produced a significant amount of hail aloft and at the surface, some of which was as large as 60 to 100 mm in diameter. The storm also exhibited many of the classic supercell characteristics, such as a rotating updraft, well-developed Bounded Weak Echo Region (BWER), large forward overhang, hook echo in the low-level reflectivity field, and large high-reflectivity core.

The WISCDYMM provided continuous spatial and temporal data which was used to explain in detail the microphysics, dynamics, kinematics, and precipitation processes of the simulated storm. Results from the Hail Category Model (HCM) simulation indicated that the model was able to successfully produce a quasi-steady supercell with the classic features listed above. Maximum updraft velocities of the simulated storm were in excess of 55 m/s. The intense updraft resulted in a BWER which was composed mainly of small water droplets with diameters less than 10 microns. The simulated supercell was found to be highly glaciated, containing a large quantity of hail embryo and graupel particles with diameters smaller than 10 mm. Most of these particles were advected by the updraft to the upper-levels of the storm and into the anvils. This served as a sink for rainfall and resulted in relatively low precipitation amounts at the surface (< 25 mm). The largest simulated hail sizes ($D > 40$ mm) had terminal velocities (> 32 m/s) which placed them in the mid-levels of the storm near the BWER. In these locations, there was significant accretion of liquid water and rimed snow as these stones were advected cyclonically by the mesocyclone through favorable growth regions. Many of the large hailstones grew from small hail and graupel which fell from the forward overhanging anvil and were drawn back into the updraft by the low-level wind field.

Fig. 1 XZ cross-section of theta-e through region of maximum updraft at 75 minutes. The updraft core consisted of undiluted air parcels from the low-level inflow which had theta-e values > 345 K. Minimum theta-e values (< 325 K) were located in the mid-levels of the tropopause (4-6 km) and in the low-level downdraft on the western flank of the storm. The storm top overshoot of more than 4 km above the tropopause (10 km AGL) is evident.

Fig. 2 XZ cross-section of radar reflectivities and storm-relative wind vectors through region of maximum updraft at 75 minutes. The Bounded Weak Echo Region (BWER) is evident on the eastern flank of the updraft. The BWER was caused by an intense updraft ($W_{\max} = 55-60$ m/s) which didn't allow the precipitating forming processes enough time to develop a radar-detectable echo at the mid-levels of the storm. Also note the large forward overhanging echo which extends more than 25 km downstream (east) of the updraft.

Fig. 3 Low-level XY cross-section of the rain water mixing ratio and absolute wind vectors at 120 minutes. The hook in the rain water field and low-level cyclonically vorticity near the updraft core (marked by an x) is vividly shown. Heaviest rainfall was located approximately 8 km northwest of the updraft core.

Fig. 4 Mid-level XY cross-section of the total hail mixing ratio and storm-relative wind vectors at 120 minutes. Maximum total hail contents were located 2-3 km west of the updraft core (marked by an x) in a region of cyclonic flow associated with the mesocyclone. The BWER is denoted by a local minimum in the total hail mixing ratio approximately 3 km east of the updraft core. The largest hailstones were located at the mid-levels of the storm near the updraft core. Small hail embryos and graupel were advected downstream to the north and east.

Fig. 5 Upper-level XY cross-section of the snow aggregate mixing ratio and storm-relative wind vectors at 120 minutes. Strong divergence at the tropopause led to an upshear anvil which extended more than 20 km to the west of the updraft. The slow terminal velocities of snow also allowed the anvil to extend more than 150 km downwind (east) of the updraft.

Fig. 6 XZ cross-section of the total hail mixing ratio and storm-relative wind vectors at 120 minutes. Evident is the advection of hail embryos and graupel from the forward overhanging anvil into the updraft core by the low-level winds. These smaller hailstones could grow to large sizes ($D > 25$ mm) if they entered regions of higher cloud liquid water contents on the flanks of the updraft.

Table 1 provides a comparison of some of the kinematic, reflectivity, and microphysical features between the simulated and observed storm.

2 AUGUST 1981, CCOPE

TIME(MIN) = 75.000

THETA-E (K)

y(km) = 26.000

cntr interval = 5.000

X-Z SLAB

HCM SIMULATION

mx/mn = 547.45 / 322.59

min cntr = 250.000

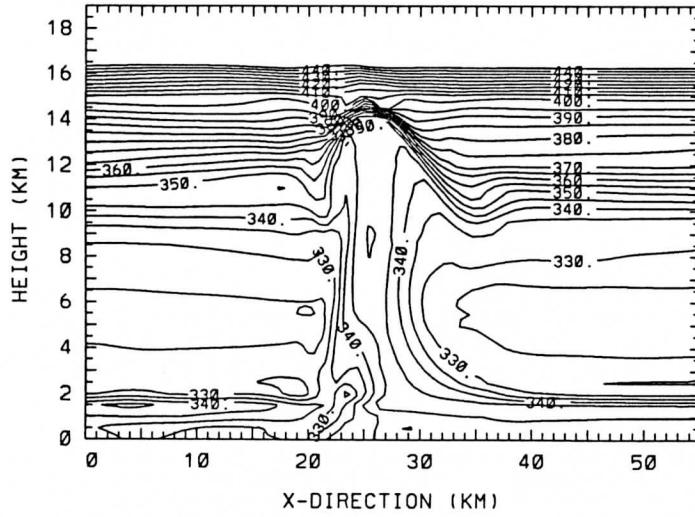


Fig. 1

2 AUGUST 1981, CCOPE

TIME(MIN) = 75.000

RADAR (DBZ)

y(km) = 26.000

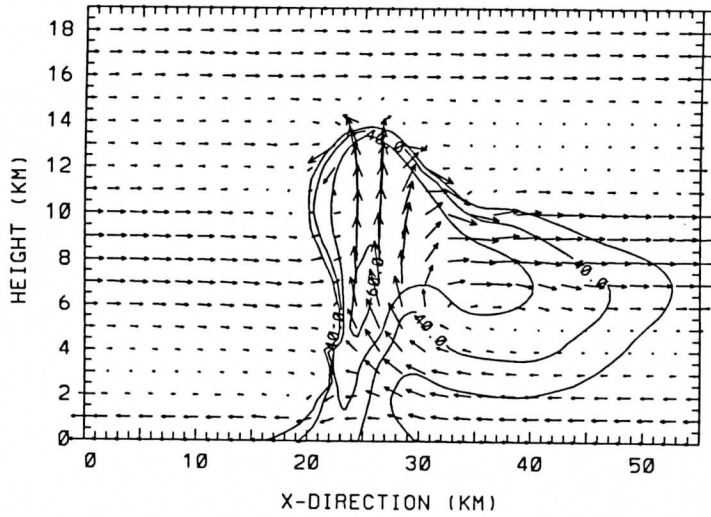
cntr interval = 10.000

X-Z SLAB

HCM SIMULATION

mx/mn = 61.70 / 0.00

min cntr = 30.000



0.575E+02
MAXIMUM VECTOR

Fig. 2

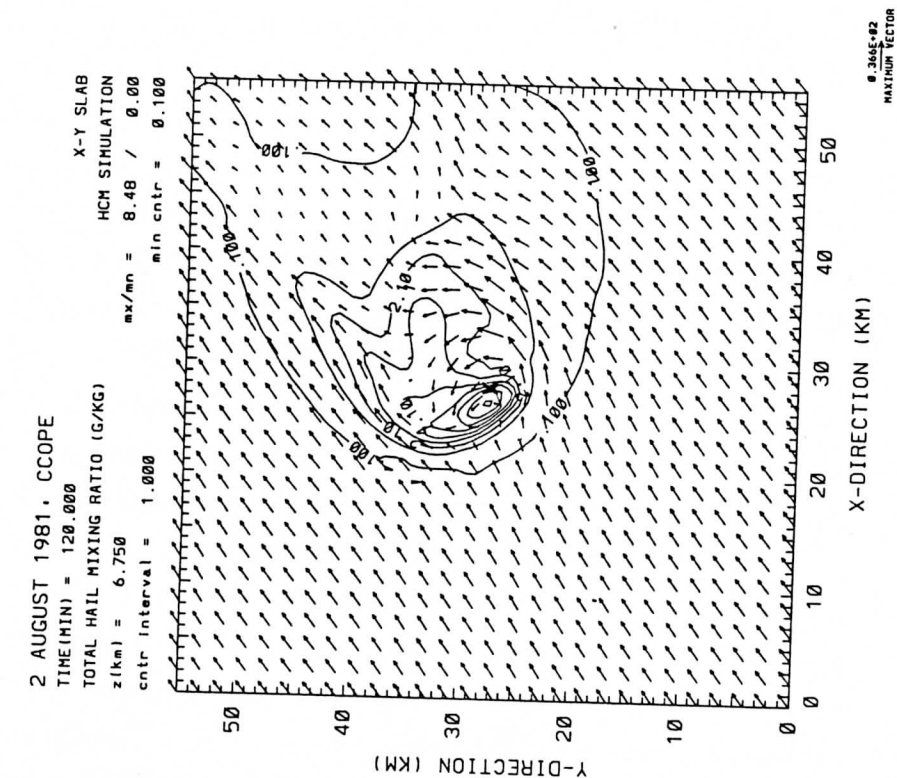


Fig.4

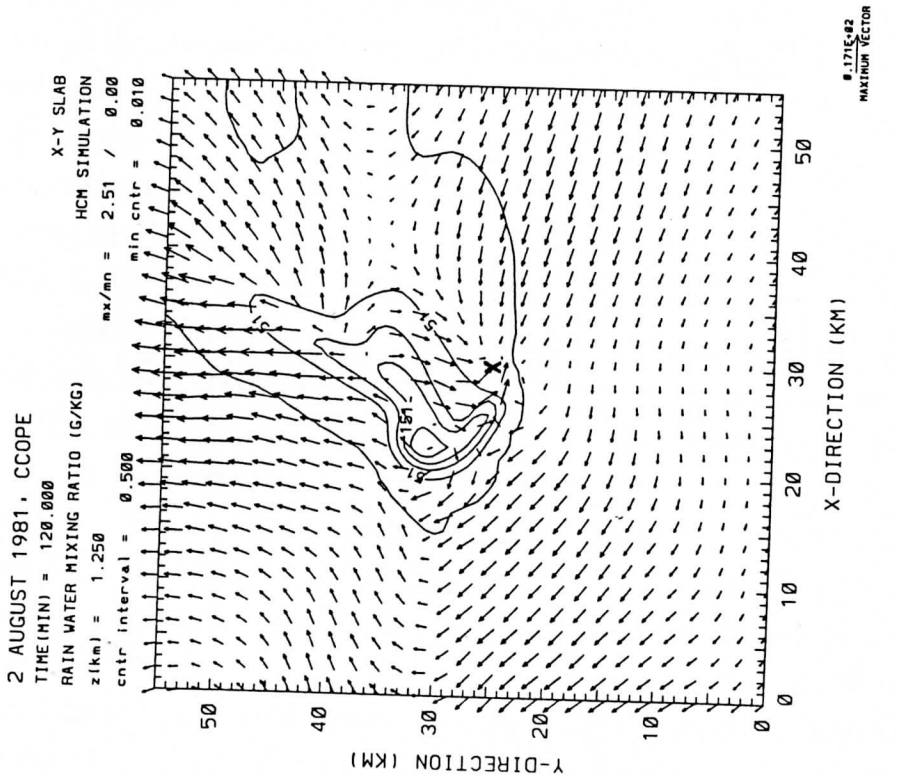


Fig.3

2 AUGUST 1981, CCOPE

TIME(MIN) = 120.000

SNOW AGGREGATE MIXING RATIO (G/KG)

z(km) = 10.250

cntr interval = 0.200

X-Y SLAB

HCM SIMULATION

mx/mn = 0.98 / 0.00

min cntr = 0.100

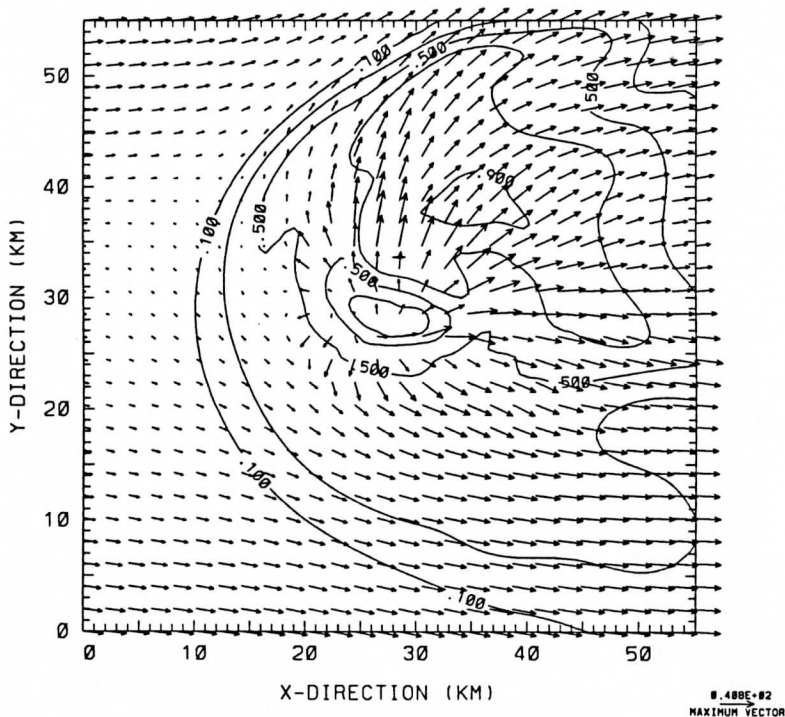


Fig. 5

2 AUGUST 1981, CCOPE

TIME(MIN) = 120.000

TOTAL HAIL MIXING RATIO (G/KG)

y(km) = 27.000

cntr interval = 1.000

X-Z SLAB

HCM SIMULATION

mx/mn = 9.18 / 0.00

min cntr = 0.100

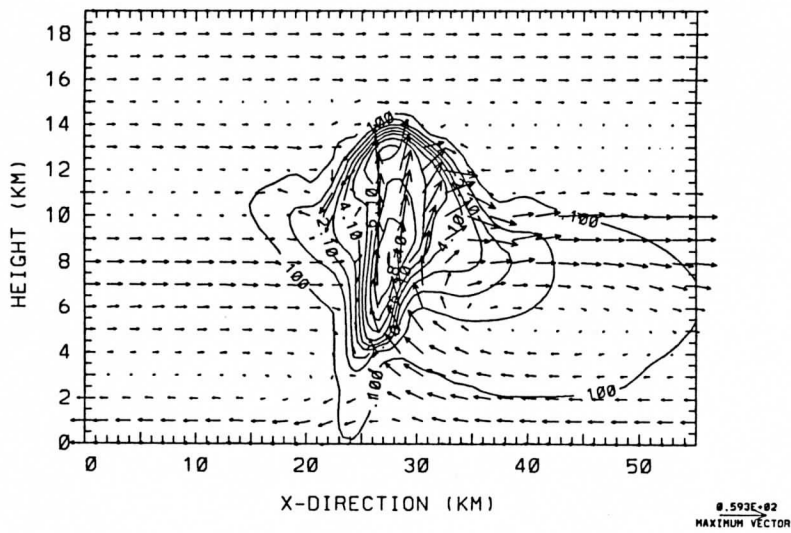


Fig. 6



Table 1

FEATURE	OBSERVATION*	SIMULATION
Anvil distance downstream from updraft	> 200 km	> 150 km**
Anvil distance upstream from updraft	> 20 km	> 20 km
BWER diameter	7 km	6-7 km
BWER vertical extent	7.5 km	7.0 km
Cloud base height	1.5 km	1.6 km
Cloud ice mixing ratio (mid-levels)	2 g/kg	1.5 g/kg
Cloud top height	14-15 km	14-15 km
Cloud water body diameter	8 km	9 km
Cloud water drop size in BWER	6 microns	4-5 microns
Cloud water mixing ratio (mid-levels)	3-4 g/kg	3-4 g/kg
Downdraft velocity (mid-levels)	12 m/s	8 m/s
Gust front location from updraft	S and E	S and E
Gust front wind velocity	> 20 m/s	> 20 m/s
Hail typical diameters at surface	10-30 mm	5-20 mm
Hail maximum diameter at surface	8.8 cm	7.3 cm
Hail shaft location from BWER	3-4 km W	3 km NW
Lifetime of supercell features	> 2 hours	> 2 hours***
Low-level hook echo position	SE flank	SE flank
Low-level vorticity initiation	after 1700	after 60 min
Rainfall totals (maximum)	30-35 mm	20-25 mm
Reflectivities (maximum)	62-72 dBZ	62-65 dBZ
Reflectivities at surface	55-65 dBZ	50-60 dBZ
Reflectivities in BWER	< 35 dBZ	< 45 dBZ
Storm movement (development stage)	260 at 10 m/s	247 at 11 m/s
Storm movement (supercell stage)	282 at 18 m/s	260 at 14 m/s
Storm overshooting top above tropopause	2-3 km	2-3 km
Theta-e in low-level cool pool	320-325 K	320-325 K
Theta-e in updraft core	348-350 K	345-350 K
Updraft diameter	14-17 km	12-16 km
Updraft velocities (maximum)	50-55 m/s	60 m/s
Vertical vorticity in mid-levels	.01 s ⁻¹	.015 s ⁻¹ Vertical
vorticity max. from updraft max.	5 km S	3.5 km SE

** Estimate

*** Using coarser resolution simulation which was carried out for four hours

*Miller, L. J., J. D. Tuttle and C. A. Knight, 1988: Airflow and hail growth in a severe northern High Plains supercell. *J. Atmos. Sci.*, **45**, 736-762.

*Musil, D. J., A. J. Heymsfield and P. L. Smith, 1986: Microphysical characteristics of a well-developed weak echo region in a High Plains supercell thunderstorm. *J. Climate Appl. Meteor.*, **25**, 1037-1051.

*Weisman, M. L., J. B. Klemp and L. J. Miller, 1983: Modeling and Doppler analysis of the CCOPE August 2 supercell storm. Preprints, *13th Conf. on Severe Local Storms*, Amer. Meteor. Soc., 223-226.